



# Advances and perspectives on one-dimensional nanostructure electrode materials for potassium-ion batteries

Zhitong Xiao<sup>1</sup>, Xuanpeng Wang<sup>2,3,\*</sup>, Jiashen Meng<sup>1</sup>, Hong Wang<sup>1,4</sup>, Yunlong Zhao<sup>5</sup>, Liqiang Mai<sup>1,3,\*</sup>

<sup>1</sup> State Key Laboratory of Advanced Technology for Materials Synthesis and Processing, Wuhan University of Technology, Luoshi Road 122, Wuhan 430070, PR China

<sup>2</sup> Department of Physical Science & Technology, School of Science, Wuhan University of Technology, Luoshi Road 122, Wuhan 430070, PR China

<sup>3</sup> Foshan Xianhu Laboratory of the Advanced Energy Science and Technology Guangdong Laboratory, Xianhu Hydrogen Valley, Foshan 528200, PR China

<sup>4</sup> Nanostructure Research Center (NRC), Wuhan University of Technology, Luoshi Road 122, Wuhan, 430070, PR China

<sup>5</sup> Advanced Technology Institute, University of Surrey, Guildford Surrey GU2 7XH, UK

Potassium-ion batteries (PIBs) have aroused considerable interest as a promising next-generation advanced large-scale energy storage system due to the abundant potassium resources and high safety. However, the  $K^+$  with large ionic radius brings restricted diffusion kinetics and severe volume expansion in electrode materials, resulting in inferior actual rate characteristics and rapid capacity fading. Designing electrode materials with one-dimensional (1D) nanostructure can effectively enhance various electrochemical properties due to the well-guided electron transfer pathways, short ionic diffusion channels and high specific surface areas. In this review, we summarize the recent research progress and achievements of 1D nanostructure electrode materials in PIBs, especially focusing on the development and application of cathode and anode materials. The nanostructure, synthetic methods, electrochemical performances and structure-performance correlation are discussed in detail. The advanced characterizations on the reaction mechanisms of 1D nanostructure electrode materials in PIBs are briefly summarized. Furthermore, the main future research directions of 1D nanostructure electrode materials are also predicted, hoping to accelerate their development into the practical PIBs market.

**Keywords:** One-dimensional nanostructure; Electrode materials; Structural-performance correlation; Potassium-ion batteries; Large-scale energy storage system

## Introduction

Lithium-ion batteries (LIBs) with the merits of high energy/power density, long lifespan and environmentally friendly are putted huge demands for the rapid developed electric vehicles, communication equipment and portable electronics [1–6]. However, the limited lithium resources and uneven global distribution unavoidably increase the costs, thus hampering their further large-scale application [7–12]. Recently, potassium-ion

batteries (PIBs) are regarded as a promising alternative to LIBs in the field of large-scale energy storage due to the high natural abundance of K reserves and similar physicochemical properties between K and Li systems [13–15]. In addition, K possesses low redox potential closed to Li (–3.040 V (Li<sup>+</sup>/Li) and –2.936 V (K<sup>+</sup>/K) vs. standard hydrogen electrode), which suggests that the PIBs can deliver the high operating voltage and energy density [16–18]. Significantly, graphite as the commercial anode for LIBs can realize the insertion and extraction of K<sup>+</sup>, indicating that the established system of LIBs can smoothly transfer to PIBs [19–23]. Moreover, the K<sup>+</sup> have higher ionic conductivity than

\* Corresponding authors.

E-mail addresses: Wang, X. (wxp122525691@whut.edu.cn), Mai, L. (mlq518@whut.edu.cn).

$\text{Li}^+$  due to the small desolvation energy and solvated cations in liquid electrolytes, which endows PIB with the elevated rate performance [24–26]. However, this technology is still in its developing stage and has encountered some obstacles. The difficulties mainly arise from the large ionic radius (1.38 Å) of  $\text{K}^+$ , which considerably decreases the diffusion kinetics and available insertion sites for  $\text{K}^+$  in the host electrode materials [27,28]. In addition, the large  $\text{K}^+$  brings the more severe volume change during potassiation/depotassiation processes, causing structural destruction of the electrode materials [29,30]. Therefore, the development of high-performance electrode materials has important significance to boost the application of PIBs.

In general, electrode materials with nanostructure can effectively shorten ionic diffusion pathways, increase electrolyte-electrode contact area and mitigate volume change, thereby greatly enhancing the electrochemical performance [31–35]. Among the various nanostructures, one-dimensional (1D) nanostructures such as nanowires, nanofibers, nanotubes, nanorods, nanobelts, *etc.* attracted particular attention due to the unique superiorities on electrode materials [36–39]. 1D nanostructure can offer facile ionic and electronic transport, which endows electrode material with high rate performance [38,40]. Moreover, the electrode material with 1D nanostructure have good strain-release property to buffer the severe volume variation during ion insertion/extraction, which effectively improves the cycling stability [41]. Significantly, the 1D nano-materials show the characteristic of ultra-long and can be assembled into interconnected networks innately, which is beneficial to the synthesis of freestanding electrode and further enhances the electrochemical performance [42]. Therefore, designing the 1D nanostructure is of great significance for enhancing the electrochemical performance of the electrode materials, and has also been widely researched and applied in secondary battery systems [42,43]. In recent years, more and more efforts have been made to study the 1D nanostructured electrode materials in PIBs [44]. However, to our best knowledge, the 1D nanostructure electrode materials in PIBs are not yet reviewed comprehensively at present.

In this review, we provide an overview of recent research achievements and an outlook for 1D nanostructure electrode materials in PIBs, focusing on the development and application of cathode and anode materials. Firstly, we briefly introduce the fundamentals of PIB and 1D nanostructure electrode materials in Section “Fundamentals of PIB and 1D nanostructure electrode materials”. Subsequently, a detailed research and application of 1D nanostructure in the cathodes, including vanadium-based oxides, manganese-based oxides and binary metal layered oxides cathode materials are presented in Section “1D nanostructure cathode materials for PIBs”. Then, the summary of the study of 1D nanostructure in the anodes, including carbon materials, transition metal chalcogenide, phosphorus-based materials, antimony/bismuth-based materials and titanium/niobium-based materials is provided in Section “1D nanostructure anode materials for PIBs”. Whereafter, the advanced characterizations on the reaction mechanisms applied in 1D PIBs electrode materials are briefly summarized in Section “Advanced characterizations on the reaction mechanisms of 1D nanostructure electrode materials in PIBs”. Finally, we pre-

sent valuable insights on the practical and scientific issues regarding the prospects of 1D nanostructure electrode materials as well as for future study on PIBs, to promote their development into the practical secondary battery market (Section “Summary and perspective”). Through these discussions, we attempt to provide profound insights into the application and research of 1D nanostructure electrode materials for PIBs.

## Fundamentals of PIB and 1D nanostructure electrode materials

### *Working principle of PIBs and reaction mechanisms of electrode materials*

The working mechanism of PIBs is similar to LIBs (Fig. 1a) [45]. Electrical energy is released/stored *via* the redox reactions at the cathode and anode side. The cathode and anode are immersed in electrolyte and coupled through a separator. The separator can avoid short circuit and provide appropriate ions transport between electrodes. When charging,  $\text{K}^+$  extracted from the cathode and inserted into the anode *via* electrolyte. The cathode is in potassium-depleted state, and the anode is in potassium-rich state. The electronic charge is supplied to the anode through an external circuit to ensure charge balance. The discharge process is just the reverse of charging.

According to reaction mechanisms, the electrode materials can be classified into three types: intercalation, conversion and alloying type materials [46]. Intercalation type materials generally possess two-dimensional or three-dimensional channels for the intercalation/de-intercalation of  $\text{K}^+$  [47]. When  $\text{K}^+$  inserted and extracted, these materials can usually maintain a stable crystalline structure, and the volume change is relatively small, thus showing good cycling performance [46]. The intercalation type materials mainly include most cathode materials (layered oxides, Prussian blue and its analogues, polyanionic compounds), some carbon anode materials and titanium-based anode materials [48]. Nevertheless, most of intercalation type materials show a low theoretical capacity and slow  $\text{K}^+$  diffusion kinetics because of the limited interstitial sites, poor reaction kinetics and large ionic radius of  $\text{K}^+$ .

The conversion type materials can react with K to change the oxidation state of at least one of the metals and generate new compounds [20]. The conversion type materials mainly include transition metal oxides, transition metal phosphides, transition metal sulfides and transition metal selenides [19]. Alloying type materials refer to some metal or metalloid materials that can react to form K-contained alloys, which mainly includes Sb, Bi, P, *etc.* [49]. The alloying and conversion type materials are usually anode material, which can deliver high theoretical capacities by the conversion and alloying reaction. However, large volume expansion and low conductivity lead to inferior cycling and rate capability, which limits their applications.

### *Advantages of 1D nanostructure electrode materials for PIBs*

1D nanostructure can provide a range of advantages for electrode materials:

- (1) The ion diffusion of 1D nanostructure is usually along the radial direction, which has a short  $\text{K}^+$  diffusion length and exhibits fast  $\text{K}^+$  diffusion kinetics [50].

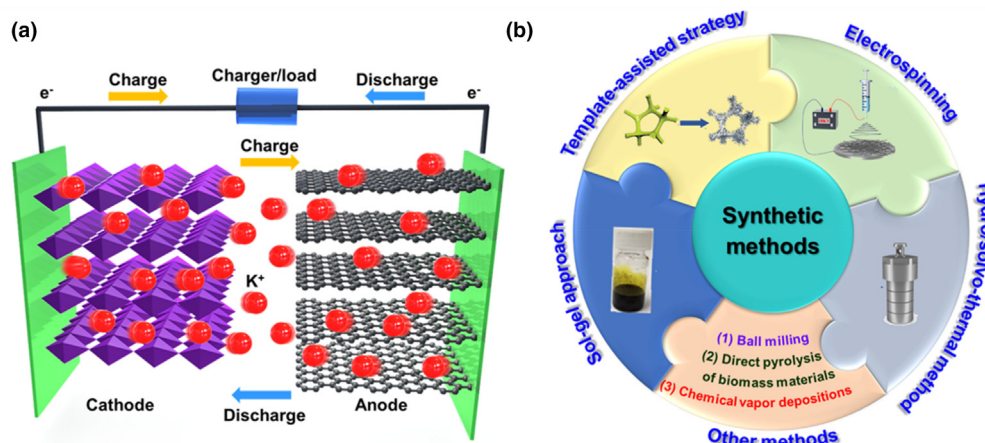


FIGURE 1

(a) Schematic illustration of PIB. (b) Main synthesis methods of 1D nanostructure electrode materials for PIBs. Reproduced with permission from Ref. [52]. Copyright 2021, Institute of Process Engineering, Chinese Academy of Sciences; from Ref. [53]. Copyright 2019, WILEY-VCH Verlag GmbH & Co. KGaA, Weinheim; from Ref. [51,54]. Copyright 2019 (2020), The Royal Society of Chemistry.

- (2) The effective strain-release property buffers the volume variation of 1D nanostructure electrode materials and enables electrode to avoid the crack even pulverization during  $K^+$  intercalation/de-intercalation process [41].
- (3) The large surface area of 1D nanostructure electrode materials provides the high electrode–electrolyte contact area, which can elevate the utilization of electrode materials and further accelerate the electrochemical reaction [36].
- (4) 1D nanostructure usually reduces the crystal size, thereby further increasing the utilization of active electrode materials in PIBs [37].
- (5) The short ion diffusion length along the radial direction and the inherent 1D continuous electron transport pathway along the axial direction make 1D nanostructure electrode materials exhibit excellent electron/ion conduction [38].
- (6) 1D ultra-long nanostructure possesses innate superiority of being assembled into interconnected networks, which can be applied to obtain the freestanding flexible electrode [42]. The freestanding electrode can be directly and conveniently implemented as the working electrode in PIBs without the use of current collector, conductive additive and binder, which can not only improve the volumetric energy and power density of the full cell, but also simplify the cell packing process [51].

#### Synthetic methods of 1D nanostructure electrode materials for PIBs

The synthesis method plays a pivotal role in nanomaterials, which is also the crucial research direction in the field of nanomaterials science [55–57]. Compared with other nanostructures, the synthesis of 1D nanostructure is unique. More attention is paid to single direction design and regulation at atomic and molecular level, so as to form the dominant growth in one direction (while inhibiting the growth in other directions), and finally obtain the target 1D nanomaterials [36]. The synthesis methods of 1D nanostructure electrode materials in PIBs, especially anode materials, are similar to that in LIBs systems. The common syn-

thesis methods of 1D PIBs electrode materials mainly include electrospinning, hydro/solvo-thermal method, template-assisted strategy, sol–gel approach and some other methods (Fig. 1b).

Electrospinning is a convenient and widely applied method to prepare 1D nanostructure electrode materials, which is also the efficient strategy to obtain complex and unique 1D nanostructure [58–60]. Compared to other methods, the electrospinning shows a number of advantages. (1) Good universality; the electrospinning method is suitable for the synthesis of most 1D nanomaterials, including cathode and anode materials, which becomes the most widely used synthesis method of 1D nanostructure electrode materials for PIBs [61–73]. For instance, the  $K_{0.7}Fe_{0.5}Mn_{0.5}O_2$  interconnected nanowires [61], N-doped porous carbon nanofibers [74],  $SnO_2$ -graphene-carbon nanofibers [75],  $SnS_2@C$  nanofibers [66],  $Co_{0.85}Se@C$  nanofibers [76] and  $Sb@C$  nanofibers [77] are all synthesized by electrospinning method. (2) Designing complex structures; by modulating the fabrication process and followed treatments, many complex nanostructures can be synthesized by electrospinning, such as multi-walled hierarchical carbon nanotube [78], necklace-like hollow carbon [63], core–shell structure  $CuS-C@Nb_2O_5-C$  nanofibers [79] and yolk-shell  $Sb@C$  nanoboxes encapsulated in carbon nanofibers [80]. (3) Easier access to freestanding electrode; the 1D nanomaterials synthesized by electrospinning usually show the ultra-long characteristic and being assembled into interconnected networks innately, which is beneficial to the synthesis of freestanding electrode [52,66,76,81,82]. However, electrospinning also suffers from some problems, such as low yield, high voltage, high cost and polymer consuming.

Hydro/solvo-thermal method is an effective route for the nanomaterials synthesizing. The application of hydrothermal method in the synthesis of 1D nanostructure electrode materials for PIBs is second only to that of electrospinning, especially in vanadium oxide materials cathode and titanium-based materials anode [83–92]. For instance,  $K_{0.5}V_2O_5$  nanobelt [85],  $(NH_4)_{0.5}V_2O_5$  nanowires [86],  $K_{1.06}Mn_8O_{16}$ /carbon nanotube (CNT) nanorods [93],  $MnO_2@reduced\ graphene\ oxide\ (rGO)$  nanowires [94],

Sb<sub>2</sub>S<sub>3</sub>@C nanowires [88], CoSe@CNTs nanotubes [89], Sb@CNT nanorods [95], K<sub>2</sub>Ti<sub>6</sub>O<sub>13</sub> nanowires [91] and T-Nb<sub>2</sub>O<sub>5</sub> nanowires [96] are all synthesized by hydro/solvo-thermal approach. However, the hydro/solvo-thermal approach of different 1D nanostructure electrode materials are not universal, and the reaction conditions and reaction parameters need to be explored, especially the complex structure, which hinders their further application.

The template-assisted approach is an effective method for synthesizing nanomaterials, especially 1D nanostructure electrode materials [97]. Yu research group [51] designed the CNT modified graphitic carbon foam (CNTs/GCF) with interconnected porous nanostructure materials *via* Ni foam as the template. Chen et al. [98] prepared the N-doped hierarchical hollow carbon nanofibers with heterogeneous distributed N-doped carbon clusters (NHCF@NCC) by MoO<sub>3</sub> nanowires as the template. The limitation is high cost, templates consuming, low yield and hard to obtain complex compositions.

Sol-gel is an approach that takes characters of the hydrolysis and polycondensation of easily hydrolyzed metal compounds in solvent, then drying and heat treatments to obtain the target product [99–101]. This method has only a few applications in 1D nanostructure electrode materials for PIBs. Jiao et al. [54] used a sol-gel approach to prepare the Bi nanorod networks encapsulated in N/S co-doped carbon matrix.

Other methods for synthesizing 1D nanostructure electrode materials include chemical vapor depositions (CVD) [81,102], direct pyrolysis of biomass materials [103–108] and ball milling [109]. For example, Yu et al. [102] developed the multiwall N-doped carbon nanotubes framework (NCNF) by a CVD approach. Jiang et al. [108] synthesized a multicore-shell Fe<sub>2</sub>N-carbon framework material *via* direct pyrolyzing the skin collagen fibers. Guo research group [109] used a ball milling method to obtain carbon fiber confined Sn<sub>4</sub>P<sub>3</sub> particles.

## 1D nanostructure cathode materials for PIBs

The reported cathode materials for PIBs mainly include: layered transition metal oxides, polyanionic compounds, Prussian blue and its analogues and organic compounds [15,16]. However, the research on 1D nanostructures in cathode materials is very scarce. So far, to our knowledge, 1D nanostructures have only been reported in vanadium-based oxides, manganese-based oxides and binary metal layered oxides cathode materials (Fig. 2). The summary of 1D nanostructure cathode materials for PIBs are provided in Table 1.

### Vanadium-based oxides

Vanadium-based oxides, including V<sub>2</sub>O<sub>5</sub>, K<sub>0.25</sub>V<sub>2</sub>O<sub>5</sub>, K<sub>0.25</sub>V<sub>2</sub>O<sub>5</sub>, KV<sub>5</sub>O<sub>13</sub>, K<sub>3</sub>V<sub>5</sub>O<sub>14</sub> and KV<sub>3</sub>O<sub>8</sub>, have aroused considerable interest as the PIBs cathode materials because of the high theoretical capacity, large interlayer spacing, multiple valence states of V ion, diverse structure and abundant reserves [84,85,110]. Deng et al. [85] synthesized a layered K<sub>0.5</sub>V<sub>2</sub>O<sub>5</sub> nanobelts by a facile hydrothermal reaction. From scanning electron microscope (SEM) and transmission electron microscope (TEM) images, the obtained K<sub>0.5</sub>V<sub>2</sub>O<sub>5</sub> shows a belt-like morphology with a 100–250 nm in width, a ~53.3 nm in average thickness and tens of

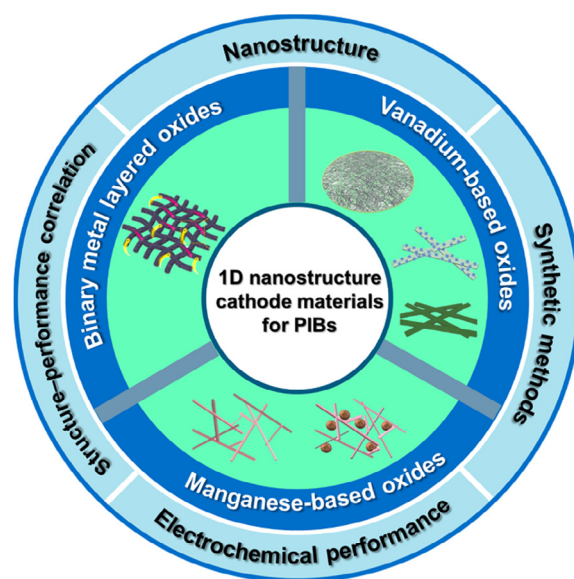


FIGURE 2

Summary of 1D nanostructure cathode materials for PIBs. Reproduced with permission from Ref. [110]. Copyright 2021, The Royal Society of Chemistry; from Ref. [53,111]. Copyright 2019, WILEY-VCH Verlag GmbH & Co. KGaA, Weinheim; from Ref. [61]. Copyright 2016, American Chemical Society.

micrometers in length (Fig. 3a, b). When measured as the PIB cathode material in 1.5–3.8 V, the K<sub>0.5</sub>V<sub>2</sub>O<sub>5</sub> nanobelts exhibited a good cycling capability with 90.3% capacity retention at 20 mA g<sup>-1</sup> after 80 cycles and a fast rate property with 60 mAh g<sup>-1</sup> at 200 mA g<sup>-1</sup> (Fig. 3c, d). Moreover, the *ex situ* X-ray photoelectron spectroscopy (XPS) and X-ray diffraction (XRD) characterizations were carried out to explore the structure evolution and K storage mechanism. The bilayered δ-K<sub>x</sub>V<sub>2</sub>O<sub>5</sub>·nH<sub>2</sub>O nanobelts was designed *via* a two-step chemically pre-intercalated synthesis approach by Clites et al. [84]. Firstly, the precursor α-V<sub>2</sub>O<sub>5</sub> powder is decomposed in aqueous solution with the presence of K<sup>+</sup> (Fig. 3e). Then, during the aging process, K<sup>+</sup> and water molecules are embedded between the vanadium oxide bilayers, which forms the δ-K<sub>x</sub>V<sub>2</sub>O<sub>5</sub>·nH<sub>2</sub>O phase (Fig. 3e). The synthesized δ-K<sub>x</sub>V<sub>2</sub>O<sub>5</sub>·nH<sub>2</sub>O shows a nanobelt morphology with a 30–100 nm in width and up to 50 μm in lengths (Fig. 3f). When measured as the PIB cathode material, δ-K<sub>x</sub>V<sub>2</sub>O<sub>5</sub>·nH<sub>2</sub>O nanobelts exhibit a high capacity of 226 mAh g<sup>-1</sup> at C/15 (~20 mA g<sup>-1</sup>) and a good cycling capability with 74% capacity retention after 50 cycles (Fig. 3g).

Although 1D nanostructure allows vanadium oxides to exhibit good potassium storage performance, they still suffer from inherently inferior electrical conductivity. Combining vanadium oxides with carbon materials can enhance the conductivity of electrode material. Li and co-workers [110] designed and synthesized a K<sub>0.5</sub>V<sub>2</sub>O<sub>5</sub>/CNT hybrid membrane consisted of CNT network and K<sub>0.5</sub>V<sub>2</sub>O<sub>5</sub> nanobelt *via* the electrostatic self-assembly and vacuum filtration process (Fig. 3h). The K<sub>0.5</sub>V<sub>2</sub>O<sub>5</sub> has a long flexible nanobelt structure with ~200 nm in width and tens of micrometers in length (Fig. 3i–k). In particular, the K<sub>0.5</sub>V<sub>2</sub>O<sub>5</sub>/CNTs films can directly serve as the cathode of flexible PIBs, without the need for current collectors and nonconductive binders (Fig. 3l). In order to expand the practical application,

TABLE 1

Summary of 1D nanostructure cathode materials for PIBs.

Cathode type	Material	Nanostructure	Synthesis method	Electrochemical performance	Freestanding electrode	Active mass loading	Reference
Vanadium-based oxides	$K_{0.5}V_2O_5$	Nanobelt	Hydrothermal method	90.3% capacity retention at 20 mA g <sup>-1</sup> after 80 cycles	No	~1 mg cm <sup>-2</sup>	[85]
	$\delta$ - $K_{0.42}V_2O_5 \cdot 0.25H_2O$	Nanobelts	Two-step chemically preintercalated	226 mAh g <sup>-1</sup> at 20 mA g <sup>-1</sup>	No	~0.37 mg cm <sup>-2</sup>	[84]
	$K_{0.5}V_2O_5/CNTs$	Nanobelts	Electrostatic self-assembly	82.2% capacity retention at 500 mA g <sup>-1</sup> over 300 cycles	Yes	~4 mg cm <sup>-2</sup>	[110]
	$\delta$ - $K_{0.51}V_2O_5$	Nanobelt	Chemical preintercalation	64 mAh g <sup>-1</sup> at 10 A g <sup>-1</sup>	No	0.5 mg cm <sup>-2</sup>	[83]
	$(NH_4)_{0.5}V_2O_5$	Nanowires	Hydrothermal method	72% capacity retention at 100 mA g <sup>-1</sup> after 200 cycles	No	2.0 mg cm <sup>-2</sup>	[86]
Manganese-based oxides	$K_{0.486}V_2O_5$	Nanobelts	Hydrothermal method	159 mAh g <sup>-1</sup> at 20 mA g <sup>-1</sup>	No	2 mg cm <sup>-2</sup>	[53]
	$K_{1.06}Mn_8O_{16}/CNT$	Nanorods	Hydrothermal method	309.4 mAh g <sup>-1</sup> at 20 mA g <sup>-1</sup>	No	1.3–2.2 mg cm <sup>-2</sup>	[93]
Binary metal layered oxides	$\delta$ - $MnO_2/KMnF_3$	Nanowires	Homogeneous precipitation method	90 mAh g <sup>-1</sup> at 100 mA g <sup>-1</sup> over 200 cycles	No	–	[111]
	$K_{0.7}Fe_{0.5}Mn_{0.5}O_2$	Interconnected nanowires	Electrospinning and followed pyrolysis	~87% capacity retention at 1000 mA g <sup>-1</sup> over 450 cycles	No	1.4–1.6 mg cm <sup>-2</sup>	[61]

cable-shaped flexible PIBs are fabricated built on hard carbon and  $K_{0.5}V_2O_5/CNTs$ , which presents good electrochemical performance and powers for a commercial light-emitting diode (LED) (Fig. 3m–o).

In addition, some works have also reported the 1D nanostructure vanadium oxide cathode. Zhu et al. [83] synthesized the single-crystal bilayered  $\delta$ - $K_{0.51}V_2O_5$  nanobelts with an optimized growth orientation ([010] orientation) and a large interlayered structure (9.5 Å) *via* chemical pre-intercalation approach. Fan and co-workers [86] developed a series of layered vanadium oxide nanowire cathodes and demonstrated the critical effect of the cation pre-intercalation on the K de-intercalation/intercalation properties. Xie research group [53] prepared the 1D  $K_{0.486}V_2O_5$  nanobelts by preinserting  $K^+$  into  $V_2O_5$  through a hydrothermal approach as the cathode materials for high-voltage PIBs.

### Manganese-based oxides

Manganese-based oxides, including a class of  $MnO_2$ , are especially suitable as electrode materials for PIBs owing to high theoretical capacity, large 1D  $K^+$  diffusion tunnels, multiple valence states of Mn ion and low cost [93,111]. Chong et al. [93] designed the  $K_{1.06}Mn_8O_{16}$  nanorod/CNT hybrids (KMO/CNT) by using a hydrothermal strategy, as both PIB anode and cathode. The pristine KMO shows morphology of nanorods with 1 μm in length and approximately 30 nm in diameter (Fig. 4a–d). The KMO nanorods are homogeneously twisted by CNT which forms KMO/CNT material arrays (Fig. 4a–d). As the cathode, the as-prepared KMO/CNT exhibits a high capacity of 309.4 mAh g<sup>-1</sup> at 20 mA g<sup>-1</sup> and remarkable rate property of 187.1 mAh g<sup>-1</sup> at 500 mA g<sup>-1</sup> (Fig. 4e, f). Moreover, the long cycling capability can also be obtained when the KMO/CNT was measured as the

anode (Fig. 4g). The good electrochemical properties are originated from the unique 1D nanostructure and well-developed conductive network. Wang et al. [111] constructed the  $\delta$ - $MnO_2/KMnF_3$ -30 (30% mass percentage of  $KMnF_3$ ) nanowires *via* precipitation method, as the PIB cathode (Fig. 4h). Different lengths of  $\delta$ - $MnO_2$  nanowires can fully utilize the short-range filling of short nanowires and cross-linking of long nanowires, leading to more stable network connectivity (Fig. 4i). In addition, the homogeneous embedding of the  $KMnF_3$  nanoparticles between  $\delta$ - $MnO_2$  nanowires can effectively mitigate the volume change (Fig. 4i). As a proof of concept, the well-designed  $\delta$ - $MnO_2/KMnF_3$ -30 exhibits good electrochemical properties (Fig. 4j).

### Binary metal layered oxides

Layered transition metal oxides ( $A_xMO_2$ , A = Li, Na, K, M = Mn, Co, Fe, Ni, etc.) are potential cathode materials for PIBs because of the high theoretical capacity and appropriate operating potential [112–114]. Generally, depending on the amount of transition metal, layered oxides can also be divided into unit, binary and multiple oxides [21,115,116]. Unit metal layered oxides focused more on the K storage mechanism of the material itself, while binary and multiple metal layered oxides can enhance electrochemical performance through synergistic effect between metal ions. Our group constructed the  $K_{0.7}Fe_{0.5}Mn_{0.5}O_2$  interconnected nanowires as the advanced PIBs cathode material, for the first time [61]. After electrospinning and followed pyrolysis under inert atmosphere, the  $K_{0.7}Fe_{0.5}Mn_{0.5}O_2$  nanocrystalline are embedded in carbon layers (Fig. 5a). From TEM image, the diameters of the individual  $K_{0.7}Fe_{0.5}Mn_{0.5}O_2$  nanowires are measured by 50–150 nm (Fig. 5b, c). When measured as the PIB cathode

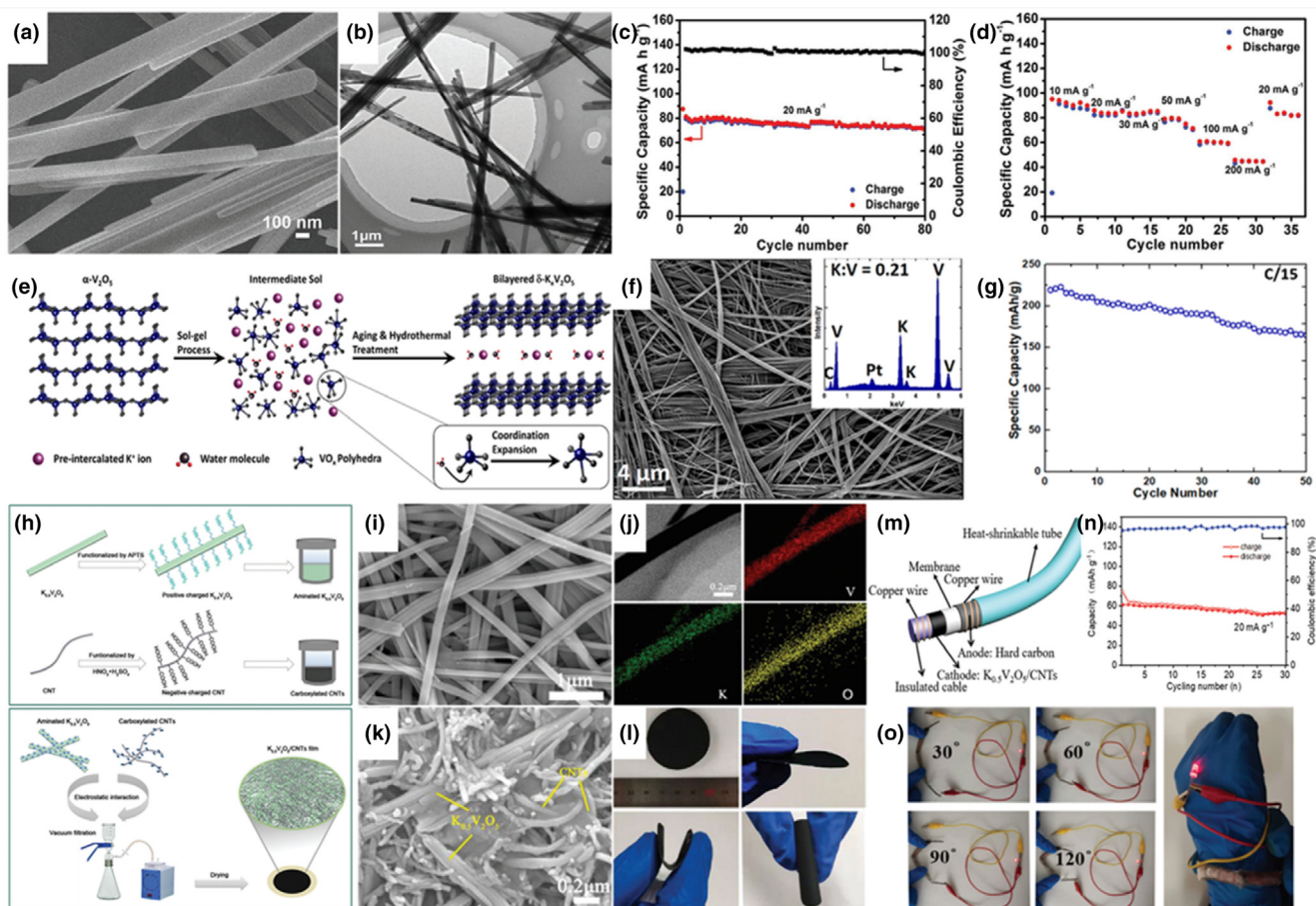


FIGURE 3

(a) SEM image, (b) TEM image, (c) cycling performance and (d) rate capability of  $K_{0.5}V_2O_5$ . Reproduced with permission from Ref. [85]. Copyright 2018, WILEY-VCH Verlag GmbH & Co. KGaA, Weinheim. (e) Schematic illustration of the chemical pre-intercalation synthesis approach of  $\delta\text{-}K_xV_2O_5 \cdot nH_2O$ . (f) SEM image and (g) cycling performance of  $\delta\text{-}K_{0.42}V_2O_5 \cdot nH_2O$  nanobelts. Reproduced with permission from Ref. [84]. Copyright 2018, American Chemical Society. (h) Schematic illustration of the  $K_{0.5}V_2O_5$ /CNTs hybrid film. (i) SEM image and (j) elemental mapping image of the  $K_{0.5}V_2O_5$  nanobelts. (k) SEM image of the  $K_{0.5}V_2O_5$ /CNTs hybrid film. (l) Optical images of the  $K_{0.5}V_2O_5$ /CNTs film at different bending states. (m) Schematic diagram and (n) cycle stability of the flexible cable-shaped PIB. (o) Photographs of a red LED powered by the cable-shaped PIBs at various bending angles. Reproduced with permission from Ref. [110]. Copyright 2021, The Royal Society of Chemistry.

material, the  $K_{0.7}Fe_{0.5}Mn_{0.5}O_2$  nanowires show superior rate capability ( $55 \text{ mAh g}^{-1}$  at  $1000 \text{ mA g}^{-1}$ ) and cycle performance (85% capacity retention at  $500 \text{ mA g}^{-1}$  over 200 cycles) (Fig. 5d, e). To demonstrate the practical application, full cells are fabricated with soft carbon anode and  $K_{0.7}Fe_{0.5}Mn_{0.5}O_2$  nanowires cathode (Fig. 5f). The full cell exhibits good rate performance with  $48 \text{ mAh g}^{-1}$  even at  $100 \text{ mA g}^{-1}$  and cycling capability with  $\sim 76\%$  capacity retention over 250 cycles (Fig. 5g, h). The remarkable electrochemical property of  $K_{0.7}Fe_{0.5}Mn_{0.5}O_2$  nanowires is ascribed to the unique 1D nanostructure, which offers continuous electron transport pathways, thus improving the conductivity.

However, there are still many other systems in binary metal layered oxides, such as Mn/Co-based, Mn/Ni-based, Mn/Mg-based, *etc.*, which have not been studied and applied by 1D nanostructure. In addition, the research state of layered oxide materials has been developed to multi-metal systems recently, which can also improve electrochemical performance by designing 1D nanostructure.

## 1D nanostructure anode materials for PIBs

The anode materials for PIBs mainly include: graphite, non-graphite carbon, metal sulfides/selenides, metal oxides, metals/alloys, and various composite materials [13,15]. The research and application of 1D nanostructures in anode materials are relatively extensive and in-depth. This section will introduce the report of 1D nanostructures in carbon materials, transition metal chalcogenide, phosphorus-based materials, antimony/bismuth-based materials and titanium/niobium-based materials (Fig. 6). The summary of 1D nanostructure anode materials for PIBs are provided in Table 2.

### Carbon materials

Carbon materials typically comprise graphite, graphene, soft carbon and hard carbon [30]. Carbon materials possess the advantages of high-conductivity, adjustable interlayer spacing, environmentally friendly and low cost [140–142]. As the commercial anode for LIBs, graphite can also allow reversible  $K^+$  insertion/extraction, showing a high capacity of  $273 \text{ mAh g}^{-1}$

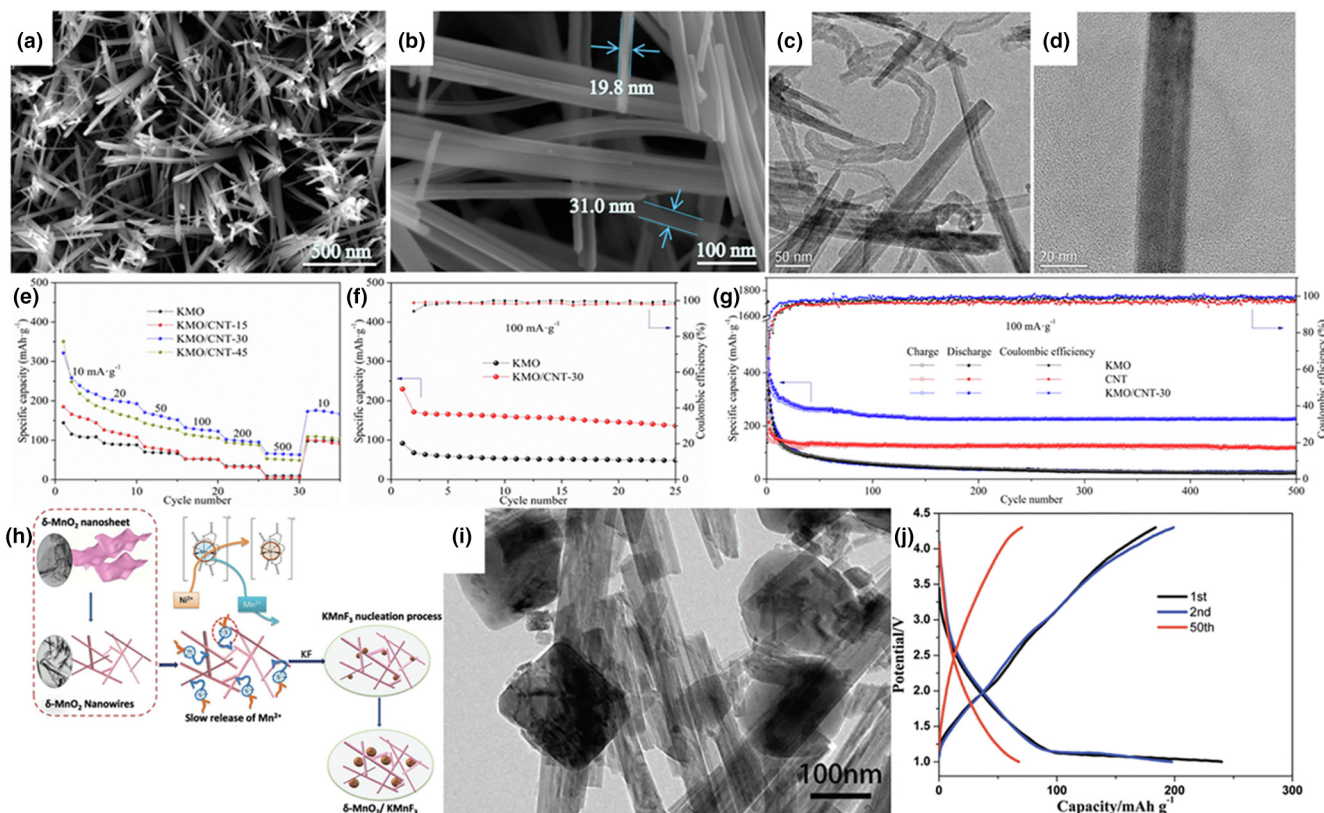


FIGURE 4

(a–d) SEM and TEM images of KMO/CNT-30. (e) Rate capability and (f) cycling properties of KMO/CNT-30 as cathode materials. (g) Cycling performance of KMO/CNT-30 as anode materials. Reproduced with permission from Ref. [93]. Copyright 2018, Elsevier Ltd. (h) Schematic synthesis process of  $\delta$ -MnO<sub>2</sub>/KMnF<sub>3</sub> composite structure. (i) TEM image and (j) charge-discharge profiles of  $\delta$ -MnO<sub>2</sub>/KMnF<sub>3</sub>-30 nanocomposite. Reproduced with permission from Ref. [111]. Copyright 2019, WILEY-VCH Verlag GmbH & Co. KGaA, Weinheim.

by forming the KC<sub>8</sub> [24]. Nevertheless, it suffers from inferior rate property and cycling capability owing to the severe volume expansion (~60%) [143]. Non-graphitic carbon materials, such as soft carbon and hard carbon, have the enlarged interlayer spacing and abundant defects, providing higher reversible capacity as anode material for PIBs [144]. Numerous studies have been devoted to adjusting the electronic structure and morphology of carbon materials for enhancing their electrochemical performance. Heteroatoms (N, S, P, O and B) doping is an effectively approach *via* increasing potassium storage sites and modifying electronic structure [62,63,118]. Designing nanostructures is other promising method to relieve the volume variation during cycling and accelerate K<sup>+</sup> diffusion [78,103].

Our group fabricated the freestanding N-doped porous carbon nanofibers (NCNFs) *via* electrospinning and followed carbonization (Fig. 7a) [74]. The chemical composition and porosity of the as-prepared NCNF can be easily controlled by modulating the heat treatment temperature and the amount of nanocrystalline templates. When heat treated at 800 °C, the NCNFs (NCNF-800) shows the morphology of nanofiber with an approximately 500 nm in average diameter (Fig. 7b). From macroscopical view, NCNF-800 is assembled into a thin freestanding nanofiber film, which can be directly applied as a bendable, binder-free and freestanding electrode (Fig. 7b). When measured as PIB anode material, NCNF-800 shows excellent long cycling capability of

150 mAh g<sup>-1</sup> at 5 A g<sup>-1</sup> even after 1000 cycles. *In situ* TEM characteristics were performed to research the morphology change of NCNF-800. NCNF-800 displays a negligible volume expansion (about 0.5%) when K<sup>+</sup> insertion, because the porous structure can efficiently maintain structural stability and moderate the volume changes (Fig. 7c-i). Although non-graphitic carbon materials exhibit the higher specific capacity, their initial Coulombic efficiency (ICE) is usually less than 60%, which are mainly ascribed to the more irreversible electrolyte consumption caused by side reactions. The construction of mesoporous in carbon materials can improve the ICE while maintaining high capacity. Recently, our group designed and constructed the mesoporous carbon nanowires *via* a simple self-etching approach (Fig. 7j) [125]. The two-step preparation contains the synthesis of Zn(Ac)<sub>2</sub>/polyvinyl alcohol (PVA) nanowires by using electrospinning and subsequently pyrolysis (Fig. 7j). The carbon-confined ZnO nanowires are used as templates and are *in situ* carbon thermally reduced to Zn metal and then evaporates, forming the homogeneous mesopores throughout the nanowires (Fig. 7k). When measured as the PIB anode material, the meso-C presents remarkable rate property of 129 mAh g<sup>-1</sup> at 2 A g<sup>-1</sup> (Fig. 7l). In particular, due to the mesoporous structure with less defects and reduced specific surface area, the meso-C exhibits a high ICE up to 76.7% (Fig. 7m). *In situ* TEM tests were performed to research the morphology change of meso-C nanowire. The diam-

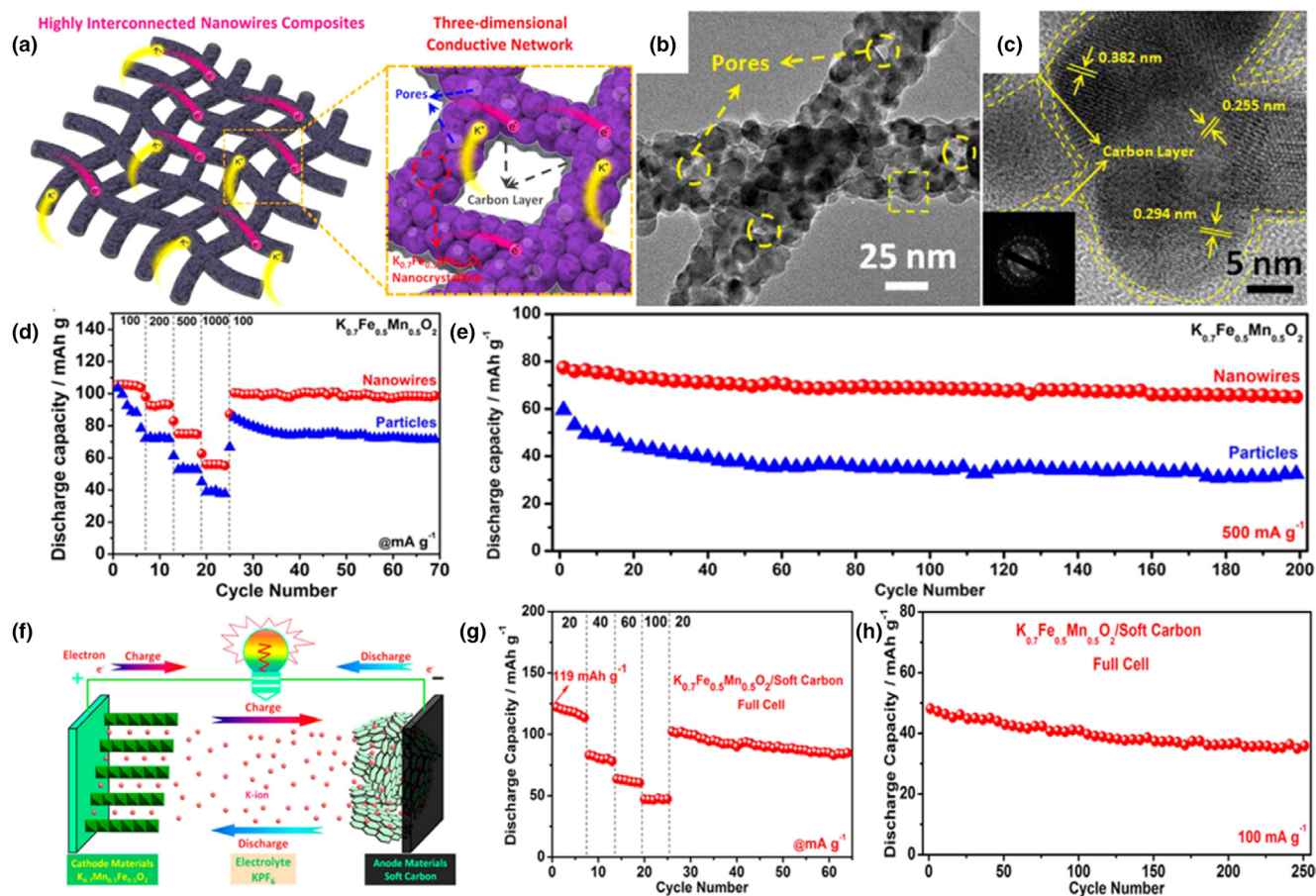


FIGURE 5

(a) Schematic illustrations, (b) TEM and (c) HRTEM images of interconnected  $K_{0.7}Fe_{0.5}Mn_{0.5}O_2$  nanowires. (d) Rate performance and (e) cycling performance for interconnected  $K_{0.7}Fe_{0.5}Mn_{0.5}O_2$  nanowires and  $K_{0.7}Fe_{0.5}Mn_{0.5}O_2$  particles in PIBs. (f) Schematic illustration, (g) rate performance and (h) cycling performance of the K-ion full cell. Reproduced with permission from Ref. [61]. Copyright 2016, American Chemical Society.

eter of meso-C nanowire shows a negligible variation during the potassiation process (Fig. 7n-p). *Ex situ* Raman measurements are further demonstrated the reversible changes in the structure of meso-C nanowire upon potassiation/depotassiation (Fig. 7q). The mesopores can accelerate  $K^+$  diffusion, facilitate the  $K^+$  adsorption on surface defects and buffer the volume change during cycling process, which greatly enhances the electrochemical property of carbon material.

In general, 1D nanostructure in carbon materials has been studied extensively. For example, the highly N-doped soft carbon nanofibers was reported by Lei research group [62], which exhibits superior rate property of  $101 \text{ mAh g}^{-1}$  at  $20 \text{ A g}^{-1}$  and cycle capability with  $146 \text{ mAh g}^{-1}$  after 4000 cycles at  $2 \text{ A g}^{-1}$ . Hu et al. [118] designed and synthesized 1D porous P/N co-doped hierarchical carbon nanofibers as a freestanding anode, which delivers outstanding rate property and cycling capability. The remarkable electrochemical property is contributed to the heteroatom P/N co-doping, hierarchical pores in the 1D structure and enlarged interlayer graphite spacing. Guo research group [63] developed a 1D hollow necklace-like ultra-high pyridinic/pyrrolic-N doped carbon material (NHC) as a freestanding anode material. Li et al. [117] synthesized a highly wrinkled N/O co-doped carbon nanotubes (NO-WCTs) by using a two-step wrinkle formation

process, which exhibits remarkable cycling performance (92.8% capacity retention over 2000 cycles at  $3 \text{ A g}^{-1}$ ).

### Transition metal chalcogenide

The transition metal chalcogenide includes transition metal oxides, transition metal sulfides and transition metal selenides [79,94,102]. These materials usually possess high theoretical specific capacity, which becomes the promising candidate for PIBs anode [65,76,145,146]. For instance,  $Sb_2S_3$  has a theoretical capacity of  $974 \text{ mAh g}^{-1}$  through a consecutive electrochemical reaction of conversion (the formation of Sb) and alloying (the formation of  $K_3Sb$ ) [67]. However, these materials still suffer from rapidly capacity degradation and inferior rate performance, which is ascribed to the destructive large volume expansion and limited ionic diffusion kinetics [71,119,147]. Therefore, designing nanostructures is of great significance to relieve the volume variation and facilitate  $K^+$  diffusion during cycling, thus enhancing the electrochemical properties.

Yang et al. [87] synthesized 1D peapod-like  $Fe_2VO_4$  nanorods embedded in porous N-doped carbon nanowires ( $Fe_2VO_4 \subset NC$  nanopeapods) as anode for PIBs (Fig. 8a). According to SEM and TEM images, the  $Fe_2VO_4 \subset NC$  nanopeapods are well-confined in porous N-doped carbon nanotubes with 210 nm in

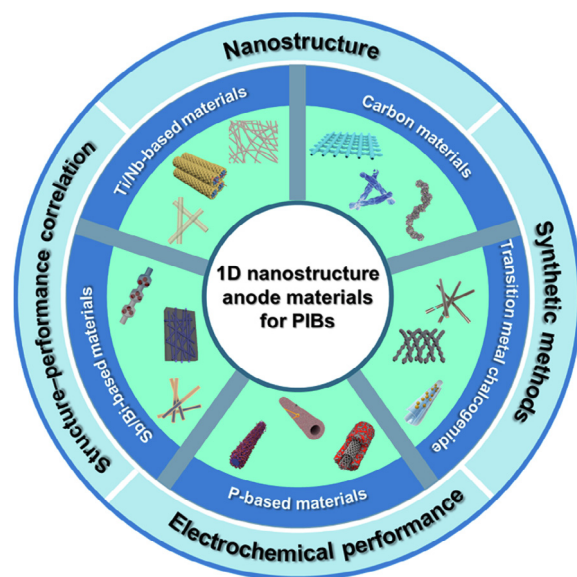


FIGURE 6

Summary of 1D nanostructure anode materials for PIBs. Reproduced with permission from Ref. [54,63,92,117-121]. Copyright 2019 (2020), The Royal Society of Chemistry; from Ref. [94,122,123]. Copyright 2018 (2019, 2020), Elsevier Ltd; from Ref. [89,124]. Copyright 2019 (2021), American Chemical Society; from Ref. [80,91]. Copyright 2018 (2020), Wiley-VCH Verlag GmbH & Co. KGaA, Weinheim.

diameter, which is intertwined in three-dimensional conductive network (Fig. 8b). As a proof of concept, the  $\text{Fe}_2\text{VO}_4 \subset \text{NC}$  electrode presents outstanding rate property of  $228 \text{ mAh g}^{-1}$  at  $2000 \text{ mA g}^{-1}$  (Fig. 8c). The unique 1D hybrid nanostructure shortens the diffusion pathways of ions/electrons and provides numerous active sites for electrochemical reactions (Fig. 8d). Moreover, Jin et al. [64] reported a flexible freestanding electrode of  $\text{V}_2\text{O}_3$  nanoparticles confined in porous N-doped carbon nanofibers ( $\text{V}_2\text{O}_3@\text{PNCNFs}$ ) via electrospinning and subsequent thermal treatment.  $\text{V}_2\text{O}_3@\text{PNCNFs}$  electrode exhibits a high capacity retention of 95.8% over 500 cycles and a good rate property of  $134 \text{ mAh g}^{-1}$  at  $1000 \text{ mA g}^{-1}$ . Huang and co-workers [75] synthesized the  $\text{SnO}_2$ -graphene-carbon ( $\text{SnO}_2\text{-G-C}$ ) nanofibers for PIB anodes, which exhibits a good rate property of  $114.81 \text{ mAh g}^{-1}$  at  $1 \text{ A g}^{-1}$  and cycle stability of  $202.06 \text{ mAh g}^{-1}$  over 100 cycles.  $\text{MnO}_2$  nanowires coated with rGO ( $\text{MnO}_2@\text{rGO}$ ) were developed by Wang and co-workers [94], which delivers a good cycling capability with capacity retention of 81.7% after 400 cycles and 75% over 500 cycles.

Ci research group [66] designed the binder-free and flexible  $\text{SnS}_2$  embedded in N,S co-doped carbon ( $\text{SnS}_2@\text{C}$ ) nanofibers via electrospinning to fabricate the foldable PIBs (Fig. 8e). By regulating the content of  $\text{SnS}_2$ , the size control of the nanofibers (280–1470 nm) and uniform distribution of  $\text{SnS}_2$  can be achieved (Fig. 8f). Notably, the binder-free freestanding  $\text{SnS}_2@\text{C}$  nanofibers membrane is remarkably flexible, which can be bending, rolling and twisting (Fig. 8g). Consequently, the  $\text{SnS}_2@\text{C}$  nanofibers exhibit high capacity of  $457.4 \text{ mAh g}^{-1}$  at  $0.05 \text{ A g}^{-1}$  and remarkable rate property of  $219.4 \text{ mAh g}^{-1}$  at  $5.0 \text{ A g}^{-1}$  (Fig. 8h). Furthermore, the foldable K-ion full batteries are established based on Prussian blue cathode and  $\text{SnS}_2@\text{C}$  anode,

demonstrating the application potential in flexible electronic equipment (Fig. 8i-k). In addition, a necklace-like composite consisted of  $\text{V}_3\text{S}_4$  microspheres confined in N-doped carbon nanofibers ( $\text{V}_3\text{S}_4@\text{NCNFs}$ ) as the PIBs anode was developed by Wu et al. [119]. Benefiting from the unique 1D structure,  $\text{V}_3\text{S}_4@\text{NCNFs}$  show a high reversible capacity of  $445 \text{ mAh g}^{-1}$  at  $0.2 \text{ A g}^{-1}$ , an outstanding cycling stability of 245  $\text{mAh g}^{-1}$  capacity retention at  $2 \text{ A g}^{-1}$  after 1000 cycles, and a superior rate property of  $202 \text{ mAh g}^{-1}$  at  $10 \text{ A g}^{-1}$ . Liu and co-workers [67] fabricated a core@shell structure  $\text{Sb}_2\text{S}_3\text{-C}@\text{Nb}_2\text{O}_5\text{-C}$  NFs via coaxial electrospinning and the subsequent treatments, which exhibits a remarkable cycling stability with 96.9% capacity retention at  $0.1 \text{ A g}^{-1}$  over 100 cycles. Du research group [128] constructed the 1D  $\text{Co}_9\text{S}_8@\text{carbon}$  nanofiber by using a electrospinning method, which displays excellent cycling capability with  $270.6 \text{ mAh g}^{-1}$  over 400 cycles and remarkable rate property with  $359.7 \text{ mAh g}^{-1}$  at  $3 \text{ A g}^{-1}$ .

The CoSe nanoparticles embedded in N-doped carbon nanotubes ( $\text{CoSe}@\text{NCNTs}$ ) as the PIB anode was designed by Huang research group [89]. The synthesis process is schematically illustrated in Fig. 8l. From SEM image, the as-prepared  $\text{CoSe}@\text{NCNTs}$  show nanowire structure and the Co nanoparticles homogeneous distribute in nanotubes (Fig. 8m). As a proof of concept,  $\text{CoSe}@\text{NCNTs}$  presents a high rate performance with  $278 \text{ mAh g}^{-1}$  at  $3.0 \text{ A g}^{-1}$  (Fig. 8n). The outstanding electrochemical capability is ascribed to two fundamental reasons. (1) The NCNT shell can relieve the volume variation of CoSe upon potassiation/depotassiation. (2) The polymer-like layer formed *in situ* on the surface of  $\text{CoSe}@\text{NCNTs}$  effectively prevents the dissolution of potassiation product  $\text{K}_2\text{Se}$  into electrolyte and enhances the reversibility of  $\text{Co}^0/\text{K}_2\text{Se}$  conversion. Chen et al. [129] constructed the  $\text{NbSe}_2$  nanosheets embedded in hierarchically N/Se co-doped porous carbon nanofibers ( $\text{NbSe}_2/\text{NSeCNFs}$ ) by electrospinning and subsequent heat treatment. The hierarchically porous nanofibers can form the conducting network, which buffers the volume variation and improves the mechanical stability and conductivity, thereby enhancing the electrochemical performance. Zhang research group [76] fabricated a flexible freestanding anode material containing with  $\text{Co}_{0.85}\text{Se}@\text{carbon}$  nanoboxes ( $\text{Co}_{0.85}\text{Se}@\text{C}$ ) encapsulated in carbon nanofibers membrane, which exhibits high capacity of  $299 \text{ mAh g}^{-1}$  at  $1 \text{ A g}^{-1}$  over 400 cycles and outstanding rate property with  $166 \text{ mAh g}^{-1}$  at  $5 \text{ A g}^{-1}$ . Xu and co-workers [130] synthesized the  $\text{V}_3\text{Se}_4$  nanoparticles confined in N/P co-doped carbon nanofibers ( $\text{V}_3\text{Se}_4/\text{NPCNFs}$ ) with a long cycling capability over 13,000 cycles.

### Phosphorus-based materials

Phosphorus-based materials include transition metal phosphides and phosphorus (P), which possess the highest theoretical capacity among the reported anode materials [29,109,148]. The transition metal phosphides can deliver high theoretical capacities by a conversion reaction to form  $\text{KP}_x$  [109,132]. Surprisingly, phosphorus shows a high theoretical capacity of  $1154 \text{ mAh g}^{-1}$  by the formation of  $\text{K}_4\text{P}_3$  [123]. Although phosphorus-based materials own significant advantages in terms of capacity, they still suffer from inferior cycle capability resulting from large volume expansion ( $\sim 200\%$  for transition metal phosphides and  $\sim 400\%$  for P) and inferior reaction kinetics caused by poor ion/electron trans-

TABLE 2

## Summary of 1D nanostructure anode materials for PIBs.

anode type	Material	Nanostructure	Synthesis method	Electrochemical performance	Freestanding electrode	Active mass loading	Reference
Carbon materials	Carbon	Coral-like nanowires	Electrospinning	93% capacity retention at 1 A g <sup>-1</sup> over 2000 cycles	Yes	4.0–5.0 mg cm <sup>-2</sup>	[52]
	Mesoporous carbon	Nanowires	Electrospinning and self-etching	70.7% capacity retention at 1 A g <sup>-1</sup> after 1000 cycles	No	~1 mg cm <sup>-2</sup>	[125]
	N/O dual-doped carbon	Highly wrinkled nanotubes	Two-step wrinkle formed method	92.8% capacity retention for 2000 cycles at 3 A g <sup>-1</sup>	No	0.8 mg cm <sup>-2</sup>	[117]
	N-doped carbon	Porous nanofibers	Electrospinning and subsequent carbonization	150 mAh g <sup>-1</sup> at 5 A g <sup>-1</sup> after 1000 cycles	Yes	2 mg cm <sup>-2</sup>	[74]
	Highly graphitized carbon	Nanofibers	Electrospinning and ultrahigh-temperature treatment	226 mAh g <sup>-1</sup> at 9765 mA g <sup>-1</sup>	Yes	1 mg cm <sup>-2</sup>	[126]
	Highly N-doped soft carbon	Nanofibers	Polypyrrole nanofibers direct carbonization	146 mAh g <sup>-1</sup> at 2 A g <sup>-1</sup> over 4000 cycles	No	~1.5 mg cm <sup>-2</sup>	[62]
	P/N co-doped carbon	Hierarchical porous nanofibers	Electrospinning and then carbonization	82.3% capacity retention at 1 A g <sup>-1</sup> after 8000 cycles	Yes	0.8–1.0 mg cm <sup>-2</sup>	[118]
	Ultra-high pyrrolic/pyridinic-N-doped carbon	Necklace-like hollow structure	Electrospinning and followed pyrolysis	161.3 mAh g <sup>-1</sup> after 1600 cycles at 1000 mA g <sup>-1</sup>	Yes	0.6–1.4 mg cm <sup>-2</sup>	[63]
	N/O co-doped hard carbon	Porous nanobelts	Carbonizing purified shrimp shells	277 mAh g <sup>-1</sup> over 1600 cycles at 1000 mA g <sup>-1</sup>	No	1.0–1.4 mg cm <sup>-2</sup>	[103]
	N-doped carbon	Cup-stacked nanotubes	Vacuum filtrating CVD-grown	75 mA h g <sup>-1</sup> at 1000 mA g <sup>-1</sup>	Yes	~1 mg cm <sup>-2</sup>	[81]
	N-doped carbon	Nanotube	Pyrolysis of polypyrrole	133 mAh g <sup>-1</sup> at 5 A g <sup>-1</sup>	Yes	~1.8 mg cm <sup>-2</sup>	[127]
	Carbon	Porous nanofibers	Electrospinning and then carbonization	100 mAh g <sup>-1</sup> at 7.7 A g <sup>-1</sup>	Yes	~1.5 mg cm <sup>-2</sup>	[82]
S/N co-doped carbon	Nanofiber aerogels	Pyrolysis of seaweed aerogels	168 mAh g <sup>-1</sup> over 1000 cycles at 2000 mA g <sup>-1</sup>	Yes	~1.4 mg cm <sup>-2</sup>	[104]	
Transition metal oxides	V <sub>2</sub> O <sub>3</sub> @PNCNFs	Nanofibers	Electrospinning and subsequent thermal treatment	95.8% capacity retention at 50 mA g <sup>-1</sup> after 500 cycles	Yes	–	[64]
	Fe <sub>2</sub> VO <sub>4</sub> ⊂ NC	Porous nanowires	Hydrothermal method and then calcination	196 mAh g <sup>-1</sup> after 2300 cycles at 4 A g <sup>-1</sup>	No	~1.2 mg cm <sup>-2</sup>	[87]
	SnO <sub>2</sub> -graphene-carbon	Nanofibers	Electrospinning	202.06 mAh g <sup>-1</sup> at 100 mA g <sup>-1</sup> over 100 cycles	No	~0.85 mg cm <sup>-2</sup>	[75]
	MnO <sub>2</sub> @rGO	Nanowires	Hydrothermal method	81.7% capacity retention at 0.2 A g <sup>-1</sup> over 400 cycles	No	1.0–1.2 mg cm <sup>-2</sup>	[94]
Transition metal sulfides	SnS <sub>2</sub> @C	Nanofibers	Electrospinning	219.4 mAh g <sup>-1</sup> at 5.0 A g <sup>-1</sup>	Yes	1.0–1.2 mg cm <sup>-2</sup>	[66]
	Sb <sub>2</sub> S <sub>3</sub> @C	Nanowires	Hydrothermal approach and followed carbonization	548 mAh g <sup>-1</sup> at 0.05 A g <sup>-1</sup>	No	0.3–0.5 mg cm <sup>-2</sup>	[88]
	V <sub>3</sub> S <sub>4</sub> @NCNFs	Nanofibers	Electrospinning and then carbonization	245 mAh g <sup>-1</sup> at 2 A g <sup>-1</sup> over 1000 cycles	No	0.8 mg cm <sup>-2</sup>	[119]
	Co <sub>9</sub> S <sub>8</sub> @C	Nanofibers	Electrospinning	359.7 mAh g <sup>-1</sup> at 3 A g <sup>-1</sup>	No	1.0–1.2 mg cm <sup>-2</sup>	[128]
Transition metal selenides	CoSe@NCNTs	Nanotubes	Hydrothermal method, carbonization and selenization	282 mAh g <sup>-1</sup> after 500 cycles at 2.0 A g <sup>-1</sup>	No	1.2 mg cm <sup>-2</sup>	[89]
	NbSe <sub>2</sub> /NSeCNFs	Nanofibers	Electrospinning and subsequent heat treatment	Over 10 000 cycles at 2 A g <sup>-1</sup>	Yes	1.5 mg cm <sup>-2</sup>	[129]
	NCNF@CoSe <sub>2</sub>	Nanotubes	Solvothermal method and selenation	173 mAh g <sup>-1</sup> over 600 cycles at 2.0 A g <sup>-1</sup>	Yes	1.5–2.0 mg cm <sup>-2</sup>	[102]

(continued on next page)

TABLE 2 (CONTINUED)

anode type	Material	Nanostructure	Synthesis method	Electrochemical performance	Freestanding electrode	Active mass loading	Reference
Transition metal phosphides	Co <sub>0.85</sub> Se@C	Nanofibers	Electrospinning and carbonization-selenidation	166 mAh g <sup>-1</sup> at 5 A g <sup>-1</sup>	Yes	0.5–1.9 mg cm <sup>-2</sup>	[76]
	V <sub>3</sub> Se <sub>4</sub> /NPCNFs	Nanofibers	Electrospinning and then carbonization	207 mAh g <sup>-1</sup> at 2 A g <sup>-1</sup> over 800 cycles	No	1.0–1.2 mg cm <sup>-2</sup>	[130]
	ZnSe@C	Nanorods	Solvothermal method and carbonization-selenidation	167.5 mAh g <sup>-1</sup> at 4.0 A g <sup>-1</sup>	No	0.9–1.4 mg cm <sup>-2</sup>	[131]
	MoP@NPCNFs	Nanofibers	Electrospinning and the later carbonization and phosphorization	220 mAh g <sup>-1</sup> at 2 A g <sup>-1</sup>	Yes	–	[70]
	Sn <sub>4</sub> P <sub>3</sub> @C	Nanofibers	Ball-milling process	160.7 mAh g <sup>-1</sup> at 500 mA g <sup>-1</sup> after 1000 cycles	No	–	[109]
	Co <sub>2</sub> P@rGO MoP@NP-HCNTs	Nanorods Nanotubes	Colloidal mesostructure method Hydrothermal method and then calcination	141 mAh g <sup>-1</sup> at 2 A g <sup>-1</sup> 463 mAh g <sup>-1</sup> at 1000 mA g <sup>-1</sup>	No No	1 mg cm <sup>-2</sup> –	[132] [90]
Phosphorus	Red P@N-PHCNFs	Nanofibers	Electrospinning and subsequent heat treatment	465 mAh g <sup>-1</sup> after 800 cycles at 2 A g <sup>-1</sup>	No	1 mg cm <sup>-2</sup>	[124]
	P@TBMC	Nanotube	Vaporization-condensation-conversion approach	~ 430 mAh g <sup>-1</sup> retained at 8 A g <sup>-1</sup>	No	0.8–1.0 mg cm <sup>-2</sup>	[123]
Antimony	P@HC u-Sb@CNFs	Nanorods Nanofibers	Vaporization-condensation-conversion Electrospinning and then carbonization	249 mAh g <sup>-1</sup> at 5 A g <sup>-1</sup> 225 mAh g <sup>-1</sup> at 1 A g <sup>-1</sup> after 2000 cycles	No Yes	1–1.2 mg cm <sup>-2</sup> 0.8 mg cm <sup>-2</sup>	[133] [134]
	Sb@CNFs	Nanofibers	Electrospinning and the later carbonization	227 mAh g <sup>-1</sup> at 1000 mA g <sup>-1</sup> over 1000 cycles	No	–	[80]
	Sb@HCT	Nanorod	Hydrothermal approach and followed carbonization	211.5 mAh g <sup>-1</sup> at 5 A g <sup>-1</sup>	No	1.2 mg cm <sup>-2</sup>	[95]
Bismuth	Sb@C PNFs Sb@CN	Nanofibers Nanofibers	Electrospinning and then carbonization Electrospinning and followed calcination	208.1 mAh g <sup>-1</sup> at 5.0 A g <sup>-1</sup> 212.7 mAh g <sup>-1</sup> at 5000 mA g <sup>-1</sup> after 1000 cycles	Yes No	~1.5 mg cm <sup>-2</sup> 0.8 mg cm <sup>-2</sup>	[135] [77]
	Bi@N-CT	Nanorods	Hydrothermal method and then carbonization	266 mAh g <sup>-1</sup> at 3850 mA g <sup>-1</sup> over 1000 cycles	No	–	[120]
	Bi ∈ NS–C	Nanorods	Sol-gel method followed by pyrolysis	91% capacity retention over 1000 cycles at 5 A g <sup>-1</sup>	No	0.8–1.0 mg cm <sup>-2</sup>	[54]
	Bi@C	Hollow nanorods	Hydrothermal method and then carbonization	80.3% capacity retention at 0.5 A g <sup>-1</sup> after 300 cycles	No	1.0–1.2 mg cm <sup>-2</sup>	[136]
Titanium-based materials	K <sub>2</sub> Ti <sub>6</sub> O <sub>13</sub> K <sub>2</sub> Ti <sub>6</sub> O <sub>13</sub>	Nanowires Nanorods	Hydrothermal method Hydrothermal method with post-sintering	120 mAh g <sup>-1</sup> at 28 mA g <sup>-1</sup> 118.5 mAh g <sup>-1</sup> for 200 cycles at 25 mA g <sup>-1</sup>	No No	0.3 mg cm <sup>-2</sup> 1.1 mg cm <sup>-2</sup>	[91] [92]
	K <sub>2</sub> Ti <sub>6</sub> O <sub>13</sub>	Nanorods	Hydrothermal method with post-sintering	95.7 mAh g <sup>-1</sup> at 0.1 A g <sup>-1</sup> over 200 times	No	~1.1 mg cm <sup>-2</sup>	[137]
	Niobium-based materials	T-Nb <sub>2</sub> O <sub>5</sub> Pb <sub>3</sub> Nb <sub>4</sub> O <sub>13</sub>	Nanowire Nanowires	Hydrothermal approach Electrospinning followed with calcination	81 mAh g <sup>-1</sup> even at 30C 74.6 mAh g <sup>-1</sup> at 50 mA g <sup>-1</sup> over 1100 cycles	No No	2 mg cm <sup>-2</sup> –
Others	Fe <sub>2</sub> N@N-CFBs	Nanofiber bundles	Direct pyrolyzing the skin collagen fibers	102 mAh g <sup>-1</sup> after 100 cycles at 200 mA g <sup>-1</sup>	No	1.0–1.2 mg cm <sup>-2</sup>	[108]
	TiO <sub>2</sub> -RP/CN	Nanofibers	Electrospinning followed with calcination	257.8 mAh g <sup>-1</sup> after 500 cycles at 0.05 A g <sup>-1</sup>	No	1.0 mg cm <sup>-2</sup>	[139]
	N-doped CoSb@C	Nanofibers	Electrospinning and then calcination	250 mAh g <sup>-1</sup> over 500 cycles at 1 A g <sup>-1</sup>	Yes	–	[72]
	Sn/N-CNFs	Nanofiber frameworks	Electrospinning followed with calcination	198.0 mAh g <sup>-1</sup> at 1 A g <sup>-1</sup> over 3000 cycles	No	0.4–0.9 mg cm <sup>-2</sup>	[73]

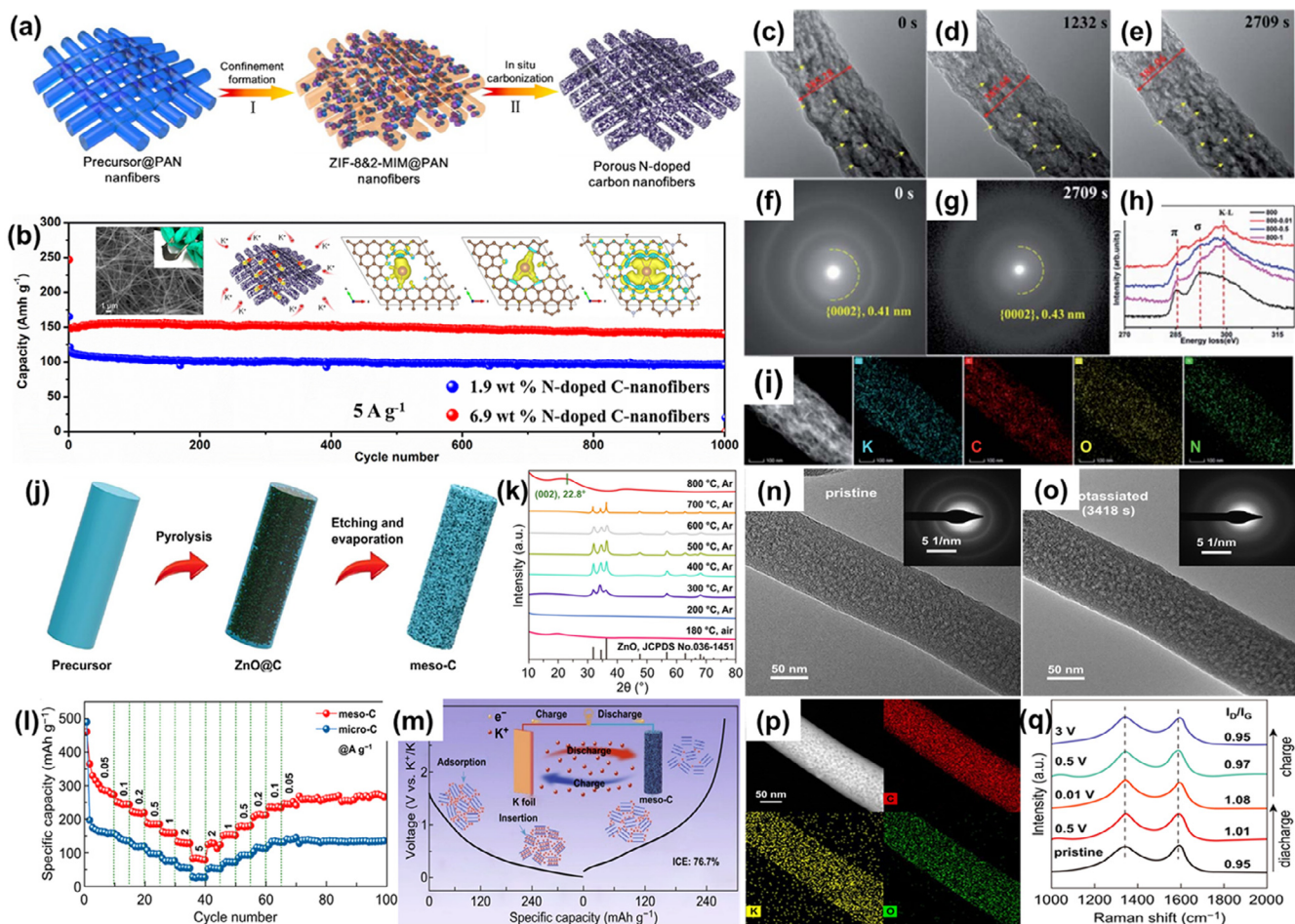


FIGURE 7

(a) Schematic illustration of the formation process of freestanding NCNF. (b) Cycling performance (inset: SEM image, optical image, K storage mechanism and theoretical calculations of NCNF-800). (c–e) The morphological evolution of NCNF-800 during the potassiation reaction. (f, g) Electron diffraction patterns of NCNF-800 before and after the potassiation reaction. (h) The *ex situ* C K-edge spectra at different states. (i) Elements mapping of potassiated NCNF-800. Reproduced with permission from Ref. [74]. Copyright 2020, The Royal Society of Chemistry. (j) Schematic diagram for the formation of meso-C. (k) Temperature-dependent *ex situ* XRD patterns of meso-C. (l) Rate performance of meso-C and micro-C. (m) Schematic illustration of K storage mechanism of meso-C. *In situ* TEM images and selected area electron diffraction (SAED) patterns of (n) pristine and (o) potassiated meso-C nanowires. (p) Elements mapping of potassiated meso-C nanowire. (q) *Ex situ* Raman spectra of meso-C. Reproduced with permission from Ref. [125]. Copyright 2020, The Author(s).

fer kinetics [29]. Therefore, designing nanostructures is of great significance to buffer the volume variation and accelerate  $K^+$  diffusion during cycling, thus enhancing the electrochemical properties.

Yi et al. [70] designed a flexible film composing of ultrafine MoP nanoparticles embedded in N/P co-doped carbon nanofibers (MoP@NPCNFs) *via* electrospinning approach with subsequent pyrolysis and phosphorization processes (Fig. 9a). The as-prepared flexible MoP@NPCNFs membrane consisted of an interconnected network of entangled, curved and rough nanofibers with around 200 nm in diameter (Fig. 9b, c). Consequently, the freestanding MoP@NPCNF electrode exhibits a more than 90% capacity retention after 200 cycles, and a superior rate capability of 220 mAh  $g^{-1}$  at 2 A  $g^{-1}$  (Fig. 9d, e). The remarkable electrochemical capability is ascribed to multiple merits: (1) The unique 1D porous structure can enhance the electrons conductivity and shorten the  $K^+$  diffuse distance. (2) The MoP ultrafine nanoparticles provide high capacity. (3) The flexibility of the MoP@NPCNFs films allows a large-scale deformation of the electrode, which can be utilized in wearable devices. Zhang and co-

workers [109] developed the  $Sn_4P_3$  confined in N-doped carbon fibers as PIB anode with improved cycling stability and fast rate property of 160.7 mAh  $g^{-1}$  at 500 mA  $g^{-1}$  after 1000 cycles. The  $Co_2P$  nanorods attached to reduced graphene oxide ( $Co_2P@rGO$ ) was constructed by Wang et al. [132], which presents a high capacity of 374 mAh  $g^{-1}$  at 20 mA  $g^{-1}$ , an outstanding rate capability of 141 mAh  $g^{-1}$  at 2 A  $g^{-1}$  and a long cycle lifespan exceeding thousands of cycles.

Yu research group [124] reported the red P nanoparticles embedded in hollow porous N-doped carbon nanofibers (red P@N-PHCNFs) (Fig. 9g). The red P@N-PHCNFs show morphology of hollow nanofiber with average outer diameter of  $\sim 350$  nm and tube wall thickness ranging from 65 to 75 nm (Fig. 9h). The red P@N-PHCNFs anode with high pore volume and large surface area can restrain the volume variation and enhance good structural stability, thereby achieving outstanding K storage performance (Fig. 9i). The morphology change of the red P@N-PHCNFs upon potassiation is explored *via in situ* TEM (Fig. 9j). During potassiated process, the red P@N-PHCNFs exhibit stable structural variation without any fracture or cracking,

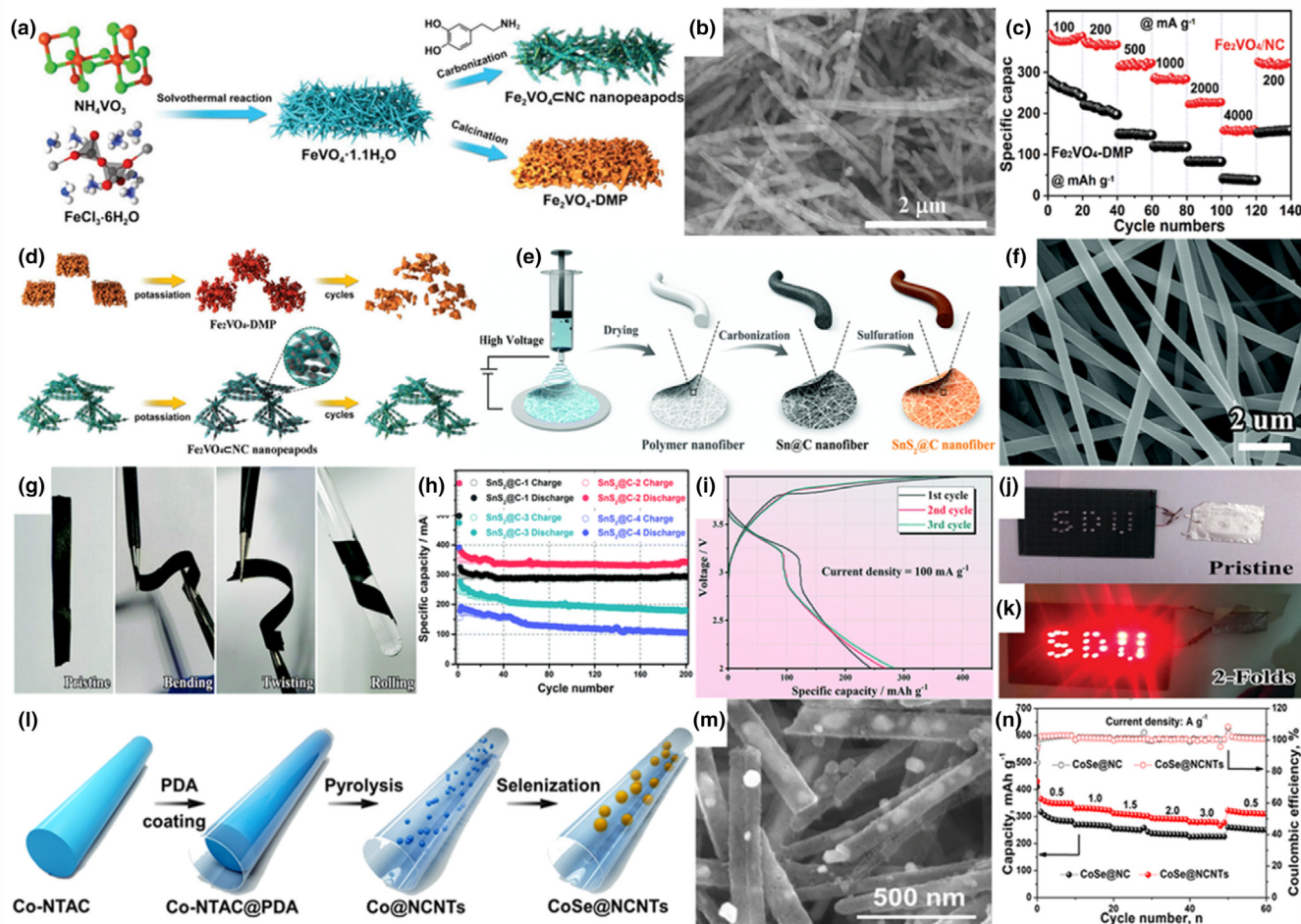


FIGURE 8

(a) Schematic illustration of the preparation process of the  $\text{Fe}_2\text{VO}_4 \text{ @ } \text{NC}$  nanopeapods. (b) SEM image and (c) rate capabilities of the  $\text{Fe}_2\text{VO}_4 \text{ @ } \text{NC}$  nanopeapods. (d) Schematic illustrations for the potassiation behaviors of  $\text{Fe}_2\text{VO}_4 \text{ @ } \text{NC}$  nanopeapods. Reproduced with permission from Ref. [87]. Copyright 2019, WILEY-VCH Verlag GmbH & Co. KGaA, Weinheim. (e) Schematic illustration of the synthetic process of  $\text{SnS}_2 \text{ @ } \text{C}$  nanofibers. (f) SEM image of  $\text{SnS}_2 \text{ @ } \text{C}$  nanofibers. (g) Demonstration of the flexible characteristic. (h) Cycling performance of  $\text{SnS}_2 \text{ @ } \text{C}$  nanofibers. (i) Charge-discharge profiles of the PIB full cell. Demonstrations of practical use by lighting LEDs: (j) pristine and (k) 2-folds. Reproduced with permission from Ref. [66]. Copyright 2021, The Royal Society of Chemistry. (l) Schematic illustration of the synthesis of  $\text{CoSe} \text{ @ } \text{NCNTs}$ . (m) SEM image and (n) rate performance of  $\text{CoSe} \text{ @ } \text{NCNTs}$ . Reproduced with permission from Ref. [89]. Copyright 2021, American Chemical Society.

which is beneficial for the excellent electrochemical performance. Liu et al. [123] designed a carbon nanotube-backed mesoporous carbon (TBMC) to impregnate the red P, forming the P@TBMC composite. The P@TBMC as an anode material for PIB displays a high capacity of  $244 \text{ mAh g}^{-1}$  at  $0.5 \text{ A g}^{-1}$  over 200 cycles. Huang and co-workers [133] synthesized a hollow C (HC) to host a high P loading of 75 wt%, which obtains the P@HC yolk/shell 1D nanostructure and shows a high capacity of  $841 \text{ mAh g}^{-1}$  with stable cycling performance.

#### Antimony/bismuth-based materials

Both antimony (Sb) and bismuth (Bi) are typical alloying type materials for PIBs anode [149,150]. Sb is a potential anode material owing to the high theoretical specific capacity ( $660 \text{ mAh g}^{-1}$ ), high electronic conductivity ( $2.56 \times 10^6 \text{ S m}^{-1}$ ), decent working voltage (0.8–0.9 V) and unusual puckered-layer structure [80,134]. Bi also shows similar strengths: high theoretical capacity ( $385 \text{ mAh g}^{-1}$ ), suitable redox potential (0.2–1 V), small voltage hysteresis and relatively flat plateaus [54,120,151].

Regrettably, the large volume expansion (about 400%) of Sb and Bi during the potassiation process causes the pulverization of electrode materials and then exfoliates from current collector, leading to rapid capacity degradation [95,136]. Therefore, optimizing the Sb and Bi to nanostructures as well as dispersing the Sb and Bi nanoparticles in an appropriate carbon host is a prospective strategy.

Zhang research group [80] prepared a hybrid structure with Sb nanoparticles encapsulated in carbon layer (Sb@C nanoboxes) wrapped in carbon nanofibers (Sb@CNFs) via an electrospinning coupled with confined ion exchange and followed carbon thermal reduction (Fig. 10a). The Sb nanoparticles are embedded in carbon nanoboxes and the Sb@C nanoboxes are strung by carbon nanofibers (Fig. 10b). When evaluated as a PIBs anode, the Sb@CNFs deliver excellent long cycling capability and rate performance (Fig. 10c). Particularly, *in situ* TEM measurement explores that the internal Sb nanoparticles experience a distinct volume variation during the potassiation and depotassiation processes (Fig. 10d). Ge et al. [134] designed a facile strategy to *in situ*

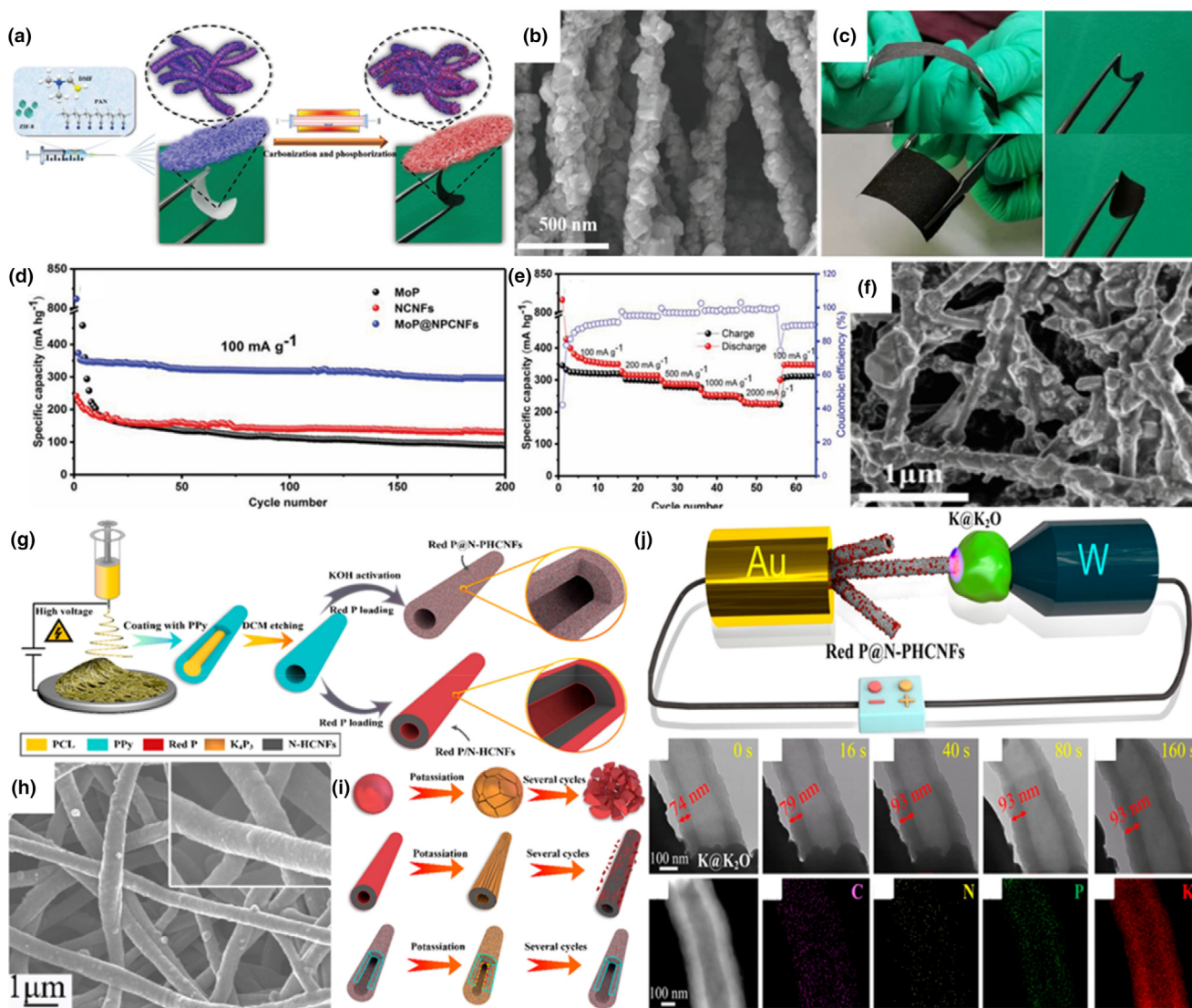


FIGURE 9

(a) Schematic illustration of the synthesis procedure of MoP@NPCNFs membrane. (b) SEM image, (c) digital images, (d) cycling performance and (e) rate performance of MoP@NPCNFs membrane. (f) SEM image of the MoP@NPCNFs electrode after cycling. Reproduced with permission from Ref. [70]. Copyright 2019, WILEY-VCH Verlag GmbH & Co. KGaA, Weinheim. (g) Schematic illustration of the synthesis process and the corresponding microstructure of the Red P@N-PHCNF and the Red P/N-HCNF. (h) SEM image of the red P@N-PHCNFs. (i) Schematic illustration of the potassiation/depotassiation process of Red P particles, Red P@N-PHCNF and the Red P/N-HCNF in PIBs. (j) Schematic illustration of the *in situ* nanobattery setup; *in situ* TEM images for P@N-PHCNFs during potassiation process; Elements mapping after full potassiation. Reproduced with permission from Ref. [124]. Copyright 2019, American Chemical Society.

wrapped ultrafine Sb nanocrystals in carbon nanofibers composed of a series of nanochannels (u-Sb@CNFs) as the anode material for PIB. The hollow 1D nanochannels and ultrasmall Sb nanocrystals enable fast  $K^+$  transport and restrain volume expansion, which endows the electrode material with remarkable electrochemical performance. Our group developed a high-performance PIB anode material composed of segment-like Sb nanorods confined in hollow carbon tubes (Sb@HCT) [95]. The unique 1D structure nanorods, sufficient inner void structure and robust carbon coating layer make the Sb@HCT exhibit the outstanding electrochemical reversibility.

Jiao et al. [54] reported a PIB anode material consisting of Bi nanorod networks encapsulated in a N/S co-doped carbon matrix ( $Bi \in NS-C$ ) through a sol-gel method and subsequent pyrolysis (Fig. 10e). The single Bi nanorods with 20–40 nm in diameter

and 100 nm in length are interconnected to form a network structure (Fig. 10f, g). Consequently, the  $Bi \in NS-C$  exhibits a high rate performance of  $289 \text{ mAh g}^{-1}$  at  $6 \text{ A g}^{-1}$  and a stable cycling property with 91% capacity retention after 1000 cycles (Fig. 10h). Moreover, the full cells fabricated by  $Bi \in NS-C$  and hexacyanoferrate ( $KMnHCFe$ ) also show a good energy density of  $295 \text{ Wh kg}^{-1}$  and an outstanding long-term cycle capability with 83% capacity retention after 800 cycles (Fig. 10i, j). The 1D structure formed network of  $Bi \in NS-C$  shortens the  $K^+$ /electrons diffusion distance, and relieves the large volume expansion upon alloying/dealloying (Fig. 10k). The Bi nanorods confined in a N-doped hollow carbon nanotube ( $Bi@N-CT$ ) was constructed by Li et al. [120], which shows a high capacity of  $316 \text{ mAh g}^{-1}$  at  $385 \text{ mA g}^{-1}$  and a remarkable rate property of  $297 \text{ mAh g}^{-1}$  at  $7700 \text{ mA g}^{-1}$ .

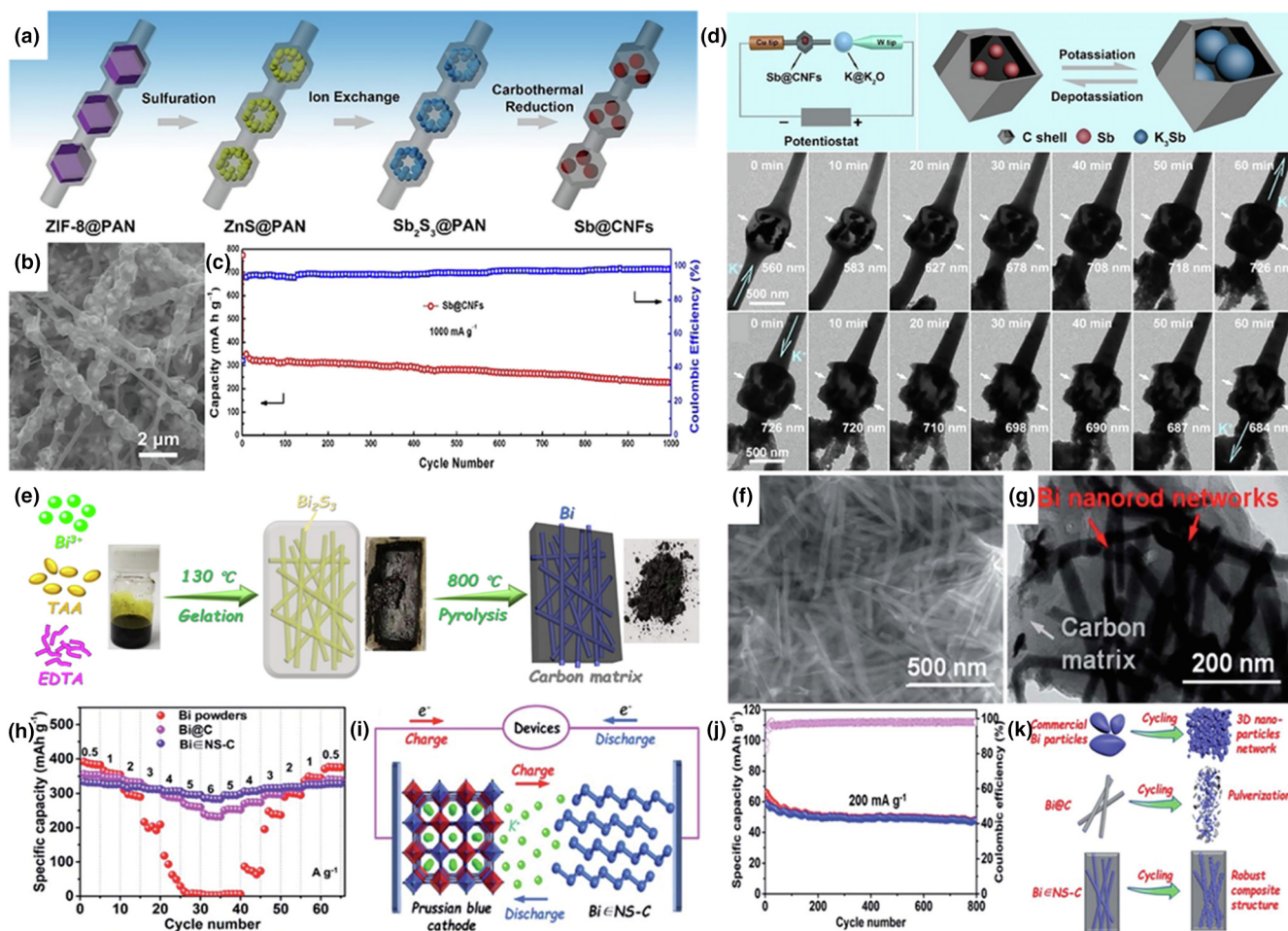


FIGURE 10

(a) Illustration of the synthesis processes for Sb@CNFs. (b) SEM image and (c) long-term cycling performance of Sb@CNFs. (d) *In situ* TEM images of single Sb@CNF during  $K^+$  during potassiation/depotassiation processes. Reproduced with permission from Ref. [80]. Copyright 2020, Wiley-VCH Verlag GmbH & Co. KGaA, Weinheim. (e) Schematic illustration of the synthesis process of Bi @ NS-C. (f) SEM image, (g) TEM image and (h) rate performance of the Bi @ NS-C. (i) Schematic illustration of KMnHCFe/Bi @ NS-C full PIBs. (j) Long-term cycling stability of the full PIBs. (k) Schematic illustrations of the morphology evolution of the different samples in the repeated alloying/dealloying process. Reproduced with permission from Ref. [54]. Copyright 2020, The Royal Society of Chemistry.

### Titanium/niobium-based materials

Titanium-based materials are representative of intercalation type anode material [15]. Various titanium-based oxides, such as  $K_2Ti_6O_{13}$ ,  $K_2Ti_4O_9$  and  $K_2Ti_8O_{17}$  have been studied for PIBs, which owns large ions transfer channels [19,91,92]. Xu et al. [91] synthesized the  $K_2Ti_6O_{13}$  nanowires with average diameters of  $\sim 5$  nm (TBTN) and  $\sim 38$  nm (TOTN) as the anode PIBs materials to research the size-dependent solid-solution reaction. TBTN shows a curled laminar morphology consisted of numerous interconnected nanowires average diameters of  $\sim 5.5$  nm (Fig. 11a, b). The TOTN and TBTN nanowires are used to investigating the insertion stress effect during potassiated process (Fig. 11c, d). Consequently, TBTN nanowires show a higher initial capacity of  $120 \text{ mAh g}^{-1}$  than TOTN with initial capacity of  $\sim 38 \text{ mAh g}^{-1}$  (Fig. 11e). The prominent high capacity is attributed to the reduction of the incoherent interface during the potassiated process (Fig. 11f, g). Maintaining the coherence interface within a single particle during  $K^+$  insertion is beneficial to the utilization and storage of coherency strain energy of solid-solution insertion material with enhanced electrochemical performance. Liu and

co-workers [92] synthesized the bunches of oriented  $K_2Ti_6O_{13}$  nanorods coated by a thin carbon layer through hydrothermal and heating treatment, which demonstrates superior cyclic stability of  $118.5 \text{ mAh g}^{-1}$  at  $25 \text{ mA g}^{-1}$  over 200 cycles.

Niobium-based materials, especially orthorhombic niobium pentoxide ( $T-Nb_2O_5$ ), possess the merits of the large interplanar lattice spacing, rapid pseudocapacitive response, good chemical stability and open intrinsic framework [15,96]. Li et al. [96] reported a  $T-Nb_2O_5$  anode material with an urchin-like hierarchical structure combined *via* nanowires (Fig. 11h, i). As a-proof of concept, the KDIB has been fabricated using  $T-Nb_2O_5$  nanowires anode and expanded graphite (EG) cathode, which presents a remarkable cycling capability with 86.2% capacity retention at 20C after 1000 cycles and a high rate property with  $81 \text{ mAh g}^{-1}$  at 30C (Fig. 11j-l).

In addition to carbon materials, transition metal chalcogenide, phosphorus-based materials, antimony/bismuth-based materials and titanium/niobium-based materials, 1D nanostructures have also been reported in some other types of anode materials in PIBs. For example, Jiang et al. [108] developed a

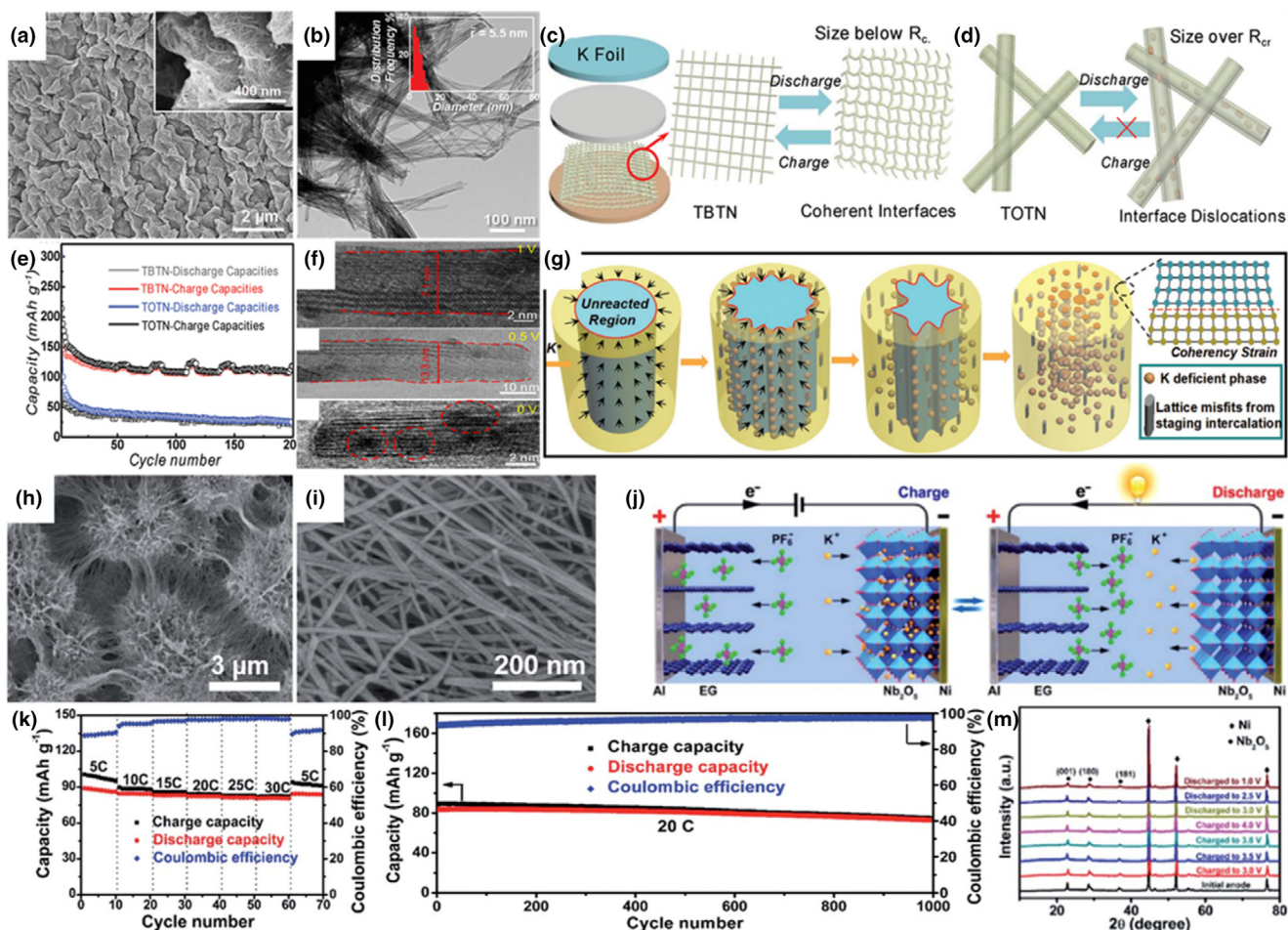


FIGURE 11

(a) SEM image and (b) TEM image of TBNT. Schematic illustrations of potassium intercalation of (c) TONT and (d) TBNT. (e) Cycling performance of TONT and TBNT. (f) HRTEM images of the potassium intercalated TBNT nanowires. (g) Schemes for the formation of the intragranular particles. Reproduced with permission from Ref. [91]. Copyright 2018, WILEY-VCH Verlag GmbH & Co. KGaA, Weinheim. (h, i) SEM images of the T-Nb<sub>2</sub>O<sub>5</sub>. (j) Schematic illustration of the working mechanism of an EG/T-Nb<sub>2</sub>O<sub>5</sub> KDIB. (k) Rate performance and (l) long-term cycling stability of the KDIB. (m) *Ex situ* XRD patterns of the T-Nb<sub>2</sub>O<sub>5</sub> anode. Reproduced with permission from Ref. [96]. Copyright 2018, The Royal Society of Chemistry.

multicore-shell framework anode *via* direct pyrolyzing the skin collagen fibers, which is composed of Fe<sub>2</sub>N nanoparticles encapsulated in N-doped carbon nanofiber bundles (Fe<sub>2</sub>N@N-CFBs). The Fe<sub>2</sub>N@N-CFBs with unique heterostructures exhibits good potassium storage performance with high reversible capacities of 242 mAh g<sup>-1</sup> at 50 mA g<sup>-1</sup>. Jiao research group [72] reported the CoSb nanoparticles confined in carbon nanofibers (N-doped CoSb@C nanofibers), which delivers remarkable cyclic stability of 250 mAh g<sup>-1</sup> at 1 A g<sup>-1</sup> over 500 cycles. Li and co-workers [73] synthesized the hybrid of N-doped carbon nanofiber frameworks encapsulated with porous Sn nanospheres (Sn/N-CNFs). When as the PIB anode, the Sn/N-CNFs show excellent cycling property of 198.0 mAh g<sup>-1</sup> after 3000 cycles at 1 A g<sup>-1</sup> (the corresponding capacity retention is 88.4%).

### Advanced characterizations on the reaction mechanisms of 1D nanostructure electrode materials in PIBs

Advanced characterization is essential to reveal the reaction mechanism and morphology-structure-performance correlation of electrode materials. Due to sophisticated battery systems, the

*ex situ* characterization cannot clearly investigate the reaction mechanism during electrochemical process [152]. *In situ* characterization can realize the real-time observation in the original position of electrode materials, which provides more direct and deeper insights in the phase transition and structure variation mechanism of electrode materials upon potassium intercalation/depotassiation. The 1D nanomaterials provide an efficient and convenient platform for the *in situ* characterization because of the unique 1D nanostructure geometry [36]. 1D nanomaterials can connect with macro- or micro-scale systems and facilitate to fabricating the monitoring equipment [153]. In addition, the freestanding 1D nanomaterials can be applied to study the high-resolution structural evolution of electrode materials without being affected by inactive materials during battery operations [154]. 1D nanomaterials have been also researched in the *in situ* characterization of PIBs, especially *in situ* TEM measurement.

#### *In situ* TEM

1D nanomaterials are beneficial to observe the morphology changes *via in situ* TEM measurement, which has been studied in electrode materials for PIBs [74,80,124,125]. The functioning

solid-state nanobattery was constructed inside the TEM for *in situ* electrochemical measurement. The *in situ* TEM technique is comprehensive, which can provide both morphology, structure (*in situ* SAED) and composition (EDS and electron energy loss spectroscopy (EELS)) information on the electrode materials and thus directly observing the structure evolution, morphology variation and ion transport during the charge/discharge process [156,157]. Wang research group [88] developed the carbon-coated  $\text{Sb}_2\text{S}_3$  ( $\text{Sb}_2\text{S}_3@\text{C}$ ) nanowires by a hydrothermal approach and subsequent carbonization. The detailed morphological variation and phase evolution of  $\text{Sb}_2\text{S}_3@\text{C}$  nanowires in real-time potassiation/depotassiation processes are comprehensively studied *via in situ* TEM measurement. The  $\text{K}^+$  diffusion, morphological variation and volume expansion of  $\text{Sb}_2\text{S}_3@\text{C}$  nanowires were clearly observed (Fig. 12a). It is concluded that the  $\text{Sb}_2\text{S}_3@\text{C}$  nanowires show small volume variation, can efficiently prevent the failure of effective electrical contact and electrode pulverization, hence improving the rate and cycling performance. Similar properties and phenomena are observed by NCNF-800 [74], meso-C [125], 3D porous CNF paper [82], red P@N-PHCNFs [124] and Sb@CNFs [80] through *in situ* TEM measurement.

Moreover, the *in situ* TEM measurement can also be combined with the *in situ* SAED test to time-resolved observe the structure evolution process of the electrode materials. The K storage mechanism is explored by *in situ* SAED measurement, which contains intercalation ( $\text{Sb}_2\text{S}_3 \rightarrow \text{K}_x\text{Sb}_2\text{S}_3$ ), conversion ( $\text{K}_x\text{Sb}_2\text{S}_3 \rightarrow \text{K}_x\text{S} + \text{Sb}$ ) and alloying reactions ( $\text{K}_x\text{S} + \text{Sb} \rightarrow \text{KSb} + \text{K}_x\text{S} \rightarrow \text{K}_3\text{Sb} + \text{K}_2\text{S}$ ) (Fig. 12b) [88]. Notably, the reaction products of  $\text{K}_2\text{S}$  and  $\text{K}_3\text{Sb}$  can be converted to the original material of  $\text{Sb}_2\text{S}_3$  after depotassiation, which implies that the electrochemical reaction of  $\text{Sb}_2\text{S}_3$  is highly reversible.

### *In situ* XRD

*In situ* XRD is widely applied to explore the structure evolution, capacity fading and energy storage mechanisms during the electrochemical process, which has a significant impact on manufacture and optimization of batteries [158]. In order to investigate the K storage mechanism of 1D nanostructure electrode material for PIBs, the *in situ* XRD technique was also employed [61,64,66,86,120]. Guo research group [109] applied *in operando* synchrotron XRD test to investigate the phase transformation processes of  $\text{Sn}_4\text{P}_3@\text{C}$  fibers (Fig. 12c). During initial discharged

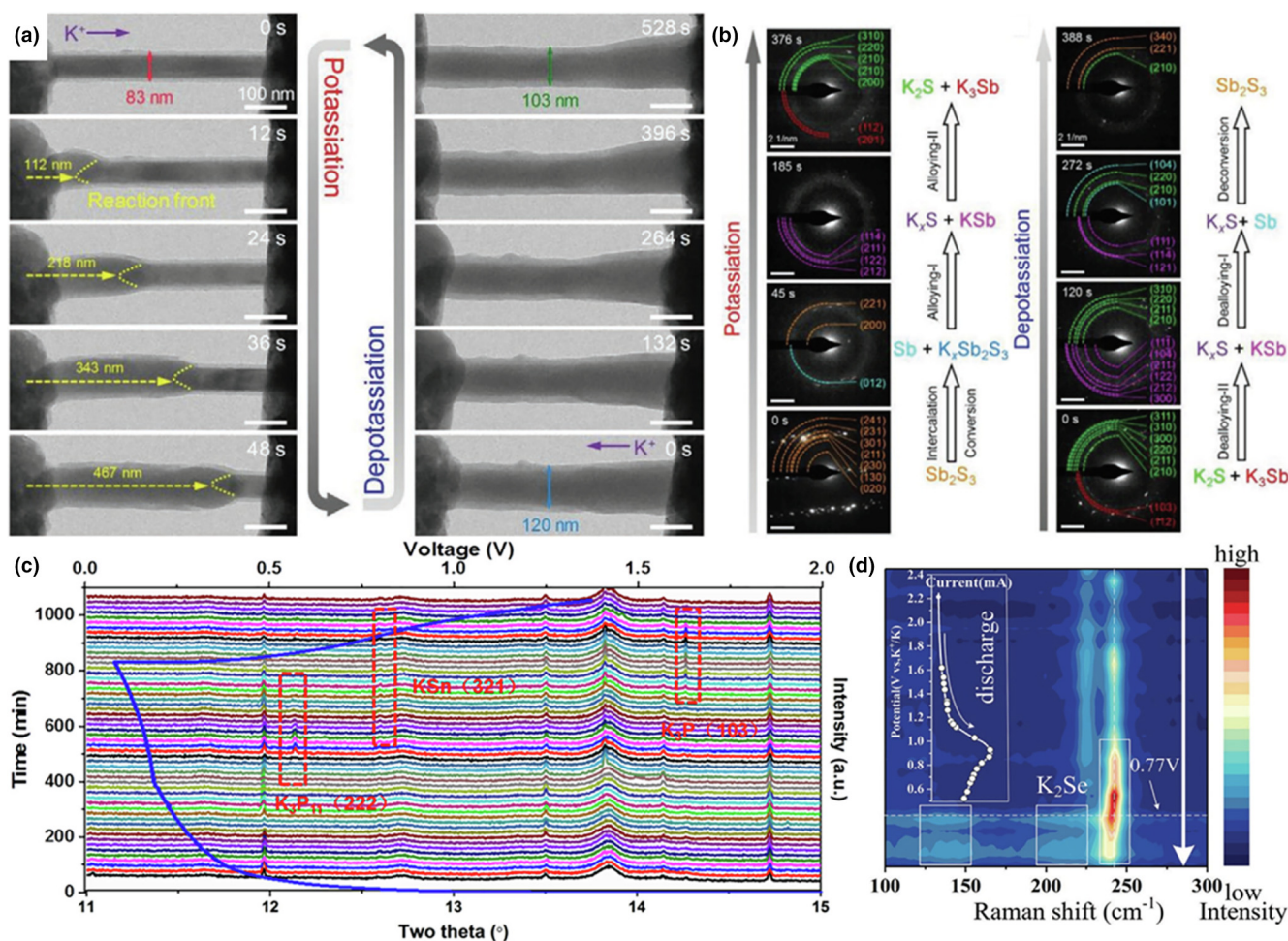


**FIGURE 12**

Time-resolved (a) *in situ* TEM images and (b) SAED patterns of  $\text{Sb}_2\text{S}_3@\text{C}$  nanowires upon potassiation and depotassiation. Reproduced with permission from Ref. [88]. Copyright 2020, Wiley-VCH GmbH. (c) *In operando* synchrotron XRD patterns of  $\text{Sn}_4\text{P}_3@\text{C}$  fibers. Reproduced with permission from Ref. [109]. Copyright 2018, Elsevier Inc. (d) Raman patterns of the  $\text{Se}@\text{NPCFs}$  during initial discharge process. Reproduced with permission from Ref. [155]. Copyright 2020, Wiley-VCH GmbH.

process, the  $\text{Sn}_4\text{P}_3$  is split to form the amorphous P and Sn metal. As followed potassiated, a conversion reaction ( $\text{P} + \text{K} \rightarrow \text{K}_3\text{P}_{11}$ ) is observed. Then,  $\text{K}_3\text{P}_{11}$  is further potassiated to form  $\text{K}_3\text{P}$  phase, Sn and K are completely alloyed to form  $\text{KSn}$  phase. Therefore, the synergistic electrochemical reactions of conversion and alloying upon potassiation create mutual buffers to relieve the volume variation. Moreover, Li et al. [66] illuminated the phase evolution of  $\text{SnS}_2@\text{C}$  nanofibers by *in situ* XRD technique. Upon potassiated, the  $\text{SnS}_2$  was reacted with K to undergo the consecutive conversion-alloying reaction and finally form the  $\text{KSn}$  alloy and  $\text{K}_2\text{S}$ , which contributes to the high reversible capacity. Chen et al. [129] used *in situ* XRD spectra to explore the phase transition of  $\text{NbSe}_2/\text{NSeCNFs}$  nanofibers. The unique reaction mechanism combining intercalation reaction ( $\text{NbSe}_2 \rightarrow \text{K}_x\text{Nb}_3\text{Se}_4$ ) and conversion reaction ( $\text{K}_x\text{Nb}_3\text{Se}_4 \rightarrow \text{K}_2\text{Se} + \text{Nb}$ ) was observed.

### *In situ* Raman spectroscopy

*In situ* Raman spectroscopy is an efficient tool for exploring the structure variation of electrode during cycling [152]. This advanced characterization has also been applied in 1D nanostructured PIBs electrode materials [51,53,126,129,135,155]. Yu research group [155] investigated the structural and compositional evolution of the Se confined in porous N-doped carbon nanofibers ( $\text{Se}@NPCFs$ ) electrode material by using *in situ* Raman spectroscopy (Fig. 12d). It is found that the short-chain molecular Se is converted into  $\text{K}_2\text{Se}$  through a “all-solid-state” two-step conversion reaction by, instead of the traditional single-step conversion process comprising dissolvable intermediate phases. Moreover, the formation of polyselenides is efficiently inhibited due to the electrochemical reaction dominated by  $\text{Se}_2$  molecule, thereby greatly improving the performance of K-Se batteries. Tian et al. [126] revealed a continuous phase variation process from  $\text{KC}_{60}$ ,  $\text{KC}_{36}$ ,  $\text{KC}_{24}$ ,  $\text{KC}_{16}$ , to  $\text{KC}_8$  during potassiation for the highly graphitized carbon nanofibers electrode *via in situ* Raman measurement. Cao and co-workers [135] confirmed the structure variation of Sb nanoparticles encapsulated into interconnecting porous carbon nanofibers ( $\text{Sb}@C$  PNFs) electrode material through *in situ* Raman test, which shows the high reversible alloying and dealloying process between  $\text{K}_3\text{Sb}$  and Sb.

In addition to *in situ* TEM, XRD and Raman spectroscopy, advanced characterizations for analyzing the reaction mechanism of 1D nanostructure electrode materials also include *in situ* SEM, *in situ* X-ray absorption spectroscopy (XAS) and *in situ* infrared spectroscopy [152]. However, to our best knowledge, these advanced characterizations have very few applications for 1D nanostructure electrode materials in PIBs to reveal the reaction mechanism at present. The advantages of 1D nanostructures in material characterization of electrode materials in PIBs have not been fully demonstrated.

### Summary and perspective

In summary, we have reviewed the recent progress and achievement of 1D nanostructures as advanced electrode materials for PIBs. The significant advantages of 1D nanostructure electrode materials in terms of their electrochemical performance are comprehensively discussed. Among the cathode materials, only vanadium-based materials, manganese-based materials and indi-

vidual binary metal layered oxides are briefly studied for 1D nanostructure. The research of 1D nanostructures in cathode materials is relatively simple and their merits have not been fully utilized. In contrast, the research of 1D nanostructure in anode materials, mainly including carbon materials, transition metal chalcogenide, phosphorus-based materials, antimony/bismuth-based materials and titanium/niobium-based materials, is extensive and in-depth. A variety of complex and unique structures are designed and obtained through efficient synthesis methods. The internal connection between 1D nanostructures and electrochemical performance of anode materials has been well demonstrated. Moreover, considerable works have made 1D nanostructured anode materials into flexible and freestanding electrode, which further enhances the electrochemical performance and practical application potential. In addition, 1D nanostructured electrode materials have also been applied to advanced characterization of PIB, mainly including *in situ* TEM, XRD and Raman test techniques, which detailed researches the morphological variation and structural evolution during cycling. In general, although numerous achievements have been made, further efforts are needed to study the 1D nanostructure electrode materials in PIBs. Herein, we outline several possible directions for 1D nanostructure electrode materials in research of PIB and hope that our perspectives will be useful to researchers in the PIB research.

#### (1) Designing and constructing special 1D nanostructures

Single-component 1D nanostructure generally cannot meet high performance requirements of electrode materials. The special 1D nanostructures mainly include core-shell structure, hierarchical/heterostructure, porous/mesoporous structure and hollow structure, which can combine multiple advantages to overcome the limitations of different electrode materials in electrochemistry. These special 1D nanostructures have been deeply studied in the electrode materials of energy storage system, but rarely reported in the PIBs electrode materials. Core-shell structure can provide more robust structure and continuous electron/ion transport channels. For example, Cui research group [159] designed the crystalline-amorphous core-shell silicon nanowires with excellent Li storage performance. The amorphous shells can store  $\text{Li}^+$  while crystalline cores function as an efficient electrical conducting pathway and a stable mechanical support. The hierarchical/heterostructure can rapidly release the strain energy caused by the volume variation, thereby endowing the electrode materials with good cycling reversibility. Our group [160] synthesized the hierarchical  $\text{MnMoO}_4/\text{CoMoO}_4$  heterostructured nanowires with enhanced supercapacitor performance. Porous/mesoporous structure can further increase the electrolyte/electrode contact area and mitigate the volume variation. Shi et al. [161] developed the highly ordered crystallized mesoporous  $\text{MoO}_2$  with highly reversible lithium storage capacity. The hollow space in the hollow structure can be loaded with other active materials and also buffer volume expansion. Lou research group [162] reported the coaxial  $\text{SnO}_2@\text{carbon}$  hollow nanospheres, which exhibits rate capabilities and exceptional cycling performance. Furthermore, the 1D nanostructure arrays, networks and bun-

dles can further enhance the comprehensive electrochemical properties.

### (2) Developing effective synthetic methods

The synthetic method is the key factor for the design of 1D nanomaterials, which is also the main reason why 1D nanostructures are not widely used in cathodes. Therefore, it is necessary to develop the effective synthesis methods to precisely control the shape and size of 1D nanomaterials (especially the special 1D nanostructures mentioned above), thus achieving the prominent improvement of electrochemical performance. Although the electrospinning method can synthesize many types of 1D nanostructured electrode materials, the yield of this method is too low to be suitable for large-scale production. Other synthesis methods usually have the restrictions on the materials type, which cannot be applied to all kinds of electrode materials. Therefore, the generality, high yield and low cost are also the requirements for the synthesis method of 1D nanostructured electrode materials. In addition, by optimizing the synthesis method, the interconnected networks composed of 1D ultra-long nanomaterial is produced, thereby obtaining freestanding flexible binder-free electrode, which further enhances the electrochemical performance and practical application prospect.

### (3) Focusing on cathode materials

According to the above summary, there are relatively few reports of 1D nanostructure cathode materials. However, less attention has been paid to several other potential materials, such as many types of layered oxides, polyanionic compounds, Prussian blue and its analogues and organic compounds. Therefore, compared with anode materials, more efforts should be devoted to the research of 1D nanostructure cathode materials. Meanwhile, the 1D nanostructure cathode nanomaterials with fine structures and the freestanding flexible cathode by using 1D nanomaterials are also rarely reported, which may be caused by the lack of suitable synthetic methods. Therefore, developing the facile approach to obtain 1D nanostructure with special fine structures and prepare them into freestanding electrode is the important research direction in the next stage of 1D cathode materials. The work of similar Li-contained and Na-contained cathode materials can provide a reference. For instance, our group [58] reported a gradient electrospinning and controlled pyrolysis approach to prepare a variety of 1D nanostructure cathode materials, including  $\text{LiNi}_{1/3}\text{Co}_{1/3}\text{Mn}_{1/3}\text{O}_2$  and  $\text{Na}_3\text{V}_2(\text{PO}_4)_3$ , mesoporous nanotubes,  $\text{Li}_3\text{V}_2(\text{PO}_4)_3$  and  $\text{Na}_{0.7}\text{Fe}_{0.7}\text{Mn}_{0.3}\text{O}_2$  pealike nanotubes.

### (4) More *in situ* characterizations

The *in situ* characterization techniques is critical for in-depth investigation of the structural evolution and morphology variation of electrode materials [163]. In an ordinary battery system, the electrode material is encapsulated in the battery, hindering its real-time observation during charge/discharge processes. *In situ* characterization can realize the real-time observation in the original position of electrode materials, which provides more direct and deeper insights in the phase transition and structure

variation mechanism of electrode materials upon potassiation/depotassiation. In particular, the 1D nanomaterials provide an efficient and convenient platform for the *in situ* characterization because of the unique 1D nanostructure geometry [36]. Moreover, the 1D nanomaterials can connect with macro- or micro-scale systems and facilitate to fabricating the monitoring equipment [153]. Some *in situ* characterizations have also been applied to the 1D nanomaterials of PIBs, mainly including *in situ* TEM, XRD and Raman test techniques. However, more *in situ* characterizations still need further application and research to analyze the reaction mechanism of 1D nanostructure electrode materials, such as *in situ* SEM, scanning transmission electron microscopy (STEM), XAS, infrared spectroscopy, *etc.* Furthermore, the 1D nanomaterials can also provide a good platform to fabricate micro/nano devices for *in situ* direct probing the electrochemical reaction mechanism, which needs to be further widely applied in PIBs [164,165].

### (5) Overcoming inherent challenge of 1D nanomaterials

As an advantage of 1D nanostructures, the large surface area of 1D nanomaterials provides a high electrode–electrolyte contact area, which can elevate the utilization rate of electrode and accelerate the electrochemical reaction. However, this advantage has also become an issue for 1D nanomaterials, which usually causes the side reactions between electrode and electrolyte and accelerate the consume of electrolyte, thus eventually leading to low Coulombic efficiency and capacity fading. In addition, the 1D nanostructure electrode materials can also decrease the tap density and volumetric energy density of the electrode, which hinder their further applications and commercialization. However, these issues are not only appeared in the 1D nanostructured electrode materials of PIBs, but also the inherent challenge of nanostructured electrode materials for other battery systems. Therefore, it is necessary to overcome this inherent challenge of nanomaterials, while long-term research and efforts are required. Fine-tuning the pore size and volume of 1D nanostructured electrode materials and designing the hierarchical/heterostructure may offers the efficient way to address this inherent challenge.

### (6) Assembling full cell based on 1D nanostructure electrode materials

In order to realize the commercialization of electrode materials, full cell assembly is necessary. In many reported works on 1D nanostructured electrode materials for PIBs, the assembly and research of full cell have been carried out, which exhibits good electrochemical performance [66,83,93,117,121,130]. However, although the studied electrode materials possess the 1D nanostructure, the matched counter electrode materials are usually the ordinary bulk materials, without considering the morphological structure. Therefore, it is an important research direction in the future to assemble full cell based on both 1D nanostructured cathode and anode materials. Furthermore, the freestanding electrode can be directly implemented as the working electrode in PIBs, which can not only improve the volumetric energy and power density of the full cell. Fabricating full-cell PIBs based on 1D freestanding flexible cathode and anode electrodes is of great

significance to further accelerate the development of 1D nanostructured electrode materials into the practical PIBs market.

All in all, the study on 1D nanostructure electrode materials in PIBs is still in the developmental stage. Therefore, it is necessary to find the solutions that connect fundamental study and commercial application. At present, most studies on 1D nanostructure materials are in the direction of electrode materials. However, in addition to the structural design of the cathode and anode materials, the research on PIBs should also focus on the balance and control the relevant parameters of the overall device of the battery, high load electrode, small pouch cell and cylindrical battery prototype. Although there are still various problems with 1D nanostructure electrode materials, the prominent achievements in recent years offer great hope for their realization in the near future.

## Notes

The authors declare no competing financial interest.

## Declaration of Competing Interest

We declare that we have no financial and personal relationships with other people or organizations that can inappropriately influence our work, there is no professional or other personal interest of any nature or kind in any product, service and/or company that could be construed as influencing the position presented in, or the review of, the manuscript entitled.

## Acknowledgements

This work was supported by the National Natural Science Foundation of China (51832004, 21905218), the National Key Research and Development Program of China (2020YFA0715000), the Natural Science Foundation of Hubei Province (2020CFB519), the Key Research and Development Program of Hubei Province (2021BAA070), the Hainan Provincial Joint Project of Sanya Yazhou Bay Science and Technology City (520LH055), the Foshan Xianhu Laboratory of the Advanced Energy Science and Technology Guangdong Laboratory (XHT2020-003), the Sanya Science and Education Innovation Park of Wuhan University of Technology (2020KF0019, 2021KF0019), and the Fundamental Research Funds for the Central Universities (WUT: 2021CG014).

## References

- [1] M. Li et al., *Adv. Mater.* 30 (2018) 1800561.
- [2] M. Winter et al., *Chem. Rev.* 118 (2018) 11433–11456.
- [3] L. Mai et al., *Nature* 546 (2017) 469–470.
- [4] M. Armand, J.-M. Tarascon, *Nature* 451 (2008) 652–657.
- [5] M. Yu et al., *Adv. Energy Mater.* 12 (2021) 2100640.
- [6] C. Jin et al., *Energy Environ. Sci.* 14 (2021) 1326–1379.
- [7] J.W. Choi, D. Aurbach, *Nat. Rev. Mater.* 1 (2016) 16013.
- [8] Y. Sun et al., *Nat. Energy* 1 (2016) 16071.
- [9] Y. Bai et al., *Mater. Today* 41 (2020) 304–315.
- [10] J.J. Roy et al., *Adv. Mater.* (2021) 2103346.
- [11] C. Lv et al., *Adv. Mater.* (2021) 2101474.
- [12] N. Zhang et al., *Chem. Soc. Rev.* 49 (2020) 4203–4219.
- [13] X. Min et al., *Energy Environ. Sci.* 14 (2021) 2186–2243.
- [14] H. Kim et al., *Adv. Energy Mater.* 8 (2018) 1702384.
- [15] T. Hosaka et al., *Chem. Rev.* 120 (2020) 6358–6466.
- [16] S. Liu et al., *Adv. Mater.* 33 (2021) 2004689.
- [17] S. Dhir et al., *Chem* 6 (2020) 2442–2460.
- [18] W. Zhang et al., *Mater. Today* 50 (2021) 400–417.
- [19] R. Rajagopalan et al., *Adv. Funct. Mater.* 30 (2020) 1909486.
- [20] J. Xu et al., *Energy Storage Mater.* 34 (2021) 85–106.
- [21] Z. Liu et al., *Energy Storage Mater.* 34 (2021) 211–228.
- [22] X. Dou et al., *Mater. Today* 23 (2019) 87–104.
- [23] C. Wu et al., *Mater. Today Energy* 19 (2021) 100595.
- [24] J.C. Pramudita et al., *Adv. Energy Mater.* 7 (2017) 1602911.
- [25] W. Zhang et al., *Sci. Adv.* 5 (2019) eaav7412.
- [26] F. Wu et al., *Mater. Today* 21 (2018) 960–973.
- [27] L. Zhang et al., *Nano Today* 37 (2021) 101074.
- [28] M. Zhou et al., *Adv. Mater.* 33 (2021) 2003741.
- [29] Y. Wu et al., *Adv. Mater.* 31 (2019) 1901414.
- [30] X. Wu et al., *Adv. Energy Mater.* 9 (2019) 1900343.
- [31] Y. Fang et al., *Matter* 1 (2019) 90–114.
- [32] F. Wang et al., *Energy Environ. Sci.* 9 (2016) 3570–3611.
- [33] Y.G. Guo et al., *Adv. Mater.* 20 (2008) 2878–2887.
- [34] Q. Zhang et al., *Chem. Soc. Rev.* 42 (2013) 3127–3171.
- [35] M. Ma et al., *Adv. Mater.* 33 (2021) 2106232.
- [36] G. Zhou et al., *Chem. Rev.* 119 (2019) 11042–11109.
- [37] Q. Wei et al., *Adv. Mater.* 29 (2017) 1602300.
- [38] L. Mai et al., *Acc. Chem. Res.* 51 (2018) 950–959.
- [39] Y. Xia et al., *Adv. Mater.* 15 (2003) 353–389.
- [40] X.-W. Lou, *Angew. Chem. Int. Ed.* 133 (2021) 20262–20278.
- [41] T. Jin et al., *Small* 14 (2018) 1703086.
- [42] K. Yu et al., *Adv. Energy Mater.* 8 (2018) 1802369.
- [43] C.K. Chan et al., *Nat. Nanotechnol.* 3 (2008) 31–35.
- [44] J. Zheng et al., *Nano-Micro Lett.* 13 (2021) 1–37.
- [45] J. Liu et al., *Mater. Today* 43 (2020) 132–165.
- [46] J. Meng et al., *Joule* 1 (2017) 522–547.
- [47] A. Eftekhari et al., *ACS Appl. Mater. Interfaces* 9 (2016) 4404–4419.
- [48] C. Zhang et al., *Adv. Funct. Mater.* 27 (2017) 1604307.
- [49] Q. Zhang et al., *Adv. Energy Mater.* 8 (2018) 1703288.
- [50] C. Wang et al., *Mater. Horiz.* 5 (2018) 394–407.
- [51] S. Zeng et al., *J. Mater. Chem. A* 7 (2019) 15774–15781.
- [52] M. Wang et al., *Green Energy Environ.* (2021), <https://doi.org/10.1016/j.gee.2021.03.007>.
- [53] K. Yuan et al., *Energy Technol.* 8 (2020) 1900796.
- [54] T. Jiao et al., *J. Mater. Chem. A* 8 (2020) 8440–8446.
- [55] L.A. Kolahalam et al., *Mater. Today: Proceed.* 18 (2019) 2182–2190.
- [56] G. Maduraiveeran et al., *Prog. Mater. Sci.* 106 (2019) 100574.
- [57] B. Ding et al., *Adv. Mater.* 32 (2020) 1905823.
- [58] C. Niu et al., *Nat. Commun.* 6 (2015) 7402.
- [59] X. Li et al., *Adv. Energy Mater.* 11 (2021) 2000845.
- [60] X. Li et al., *Adv. Energy Mater.* 11 (2021) 2170010.
- [61] X. Wang et al., *Nano Lett.* 17 (2017) 544–550.
- [62] Y. Xu et al., *Nat. Commun.* 9 (2018) 1720.
- [63] W. Yang et al., *Energy Environ. Sci.* 12 (2019) 1605–1612.
- [64] T. Jin et al., *Nano Energy* 50 (2018) 462–467.
- [65] W. Miao et al., *J. Mater. Chem. A* 7 (2019) 5504–5512.
- [66] D. Li et al., *Energy Environ. Sci.* 14 (2021) 424–436.
- [67] H. Liu et al., *Small* 17 (2021) 2008133.
- [68] Z. Tian et al., *Energy Storage Mater.* 27 (2020) 591–598.
- [69] Q. Shen et al., *Nanoscale* 11 (2019) 13511–13520.
- [70] Z. Yi et al., *Small* 16 (2020) 1905301.
- [71] C. Lai et al., *J. Mater. Chem. A* 9 (2021) 1487–1494.
- [72] J. Han et al., *J. Mater. Chem. A* 7 (2019) 25268–25273.
- [73] C. Li et al., *J. Mater. Chem. A* 9 (2021) 5740–5750.
- [74] F. Liu et al., *J. Mater. Chem. A* 8 (2020) 18079–18086.
- [75] Z. Huang et al., *Mater. Lett.* 219 (2018) 19–22.
- [76] C.A. Etogo et al., *Energy Storage Mater.* 24 (2020) 167–176.
- [77] D. Liu et al., *Sci. Bull.* 65 (2020) 1003–1012.
- [78] Y. Wang et al., *Adv. Mater.* 30 (2018) 1802074.
- [79] K. Cao et al., *Adv. Funct. Mater.* 30 (2020) 2007712.
- [80] H. Huang et al., *Angew. Chem., Int. Ed.* 132 (2020) 14612–14618.
- [81] X. Zhao et al., *ACS Appl. Energy Mater.* 1 (2018) 1703–1707.
- [82] X. Zhao et al., *J. Mater. Chem. A* 5 (2017) 19237–19244.
- [83] Y.-H. Zhu et al., *Chem* 5 (2019) 168–179.
- [84] M. Clites et al., *ACS Energy Lett.* 3 (2018) 562–567.
- [85] L. Deng et al., *Adv. Funct. Mater.* 28 (2018) 1800670.
- [86] Y. Fan et al., *ACS Appl. Mater. Interfaces* 13 (2021) 7377–7388.
- [87] C. Yang et al., *Adv. Energy Mater.* 9 (2019) 1902674.
- [88] Y. Cheng et al., *Adv. Funct. Mater.* 30 (2020) 2005417.
- [89] Y. Liu et al., *ACS Nano* 15 (2021) 1121–1132.
- [90] Z. Wang et al., *J. Colloid Interface Sci.* 584 (2021) 875–884.
- [91] S.M. Xu et al., *Adv. Energy Mater.* 8 (2018) 1802175.

- [92] C. Liu et al., *Nanoscale* 12 (2020) 11427–11434.
- [93] S. Chong et al., *Nano Energy* 54 (2018) 106–115.
- [94] Z. Wang et al., *Carbon* 174 (2021) 556–566.
- [95] W. Luo et al., *Nano Res.* 12 (2019) 1025–1031.
- [96] N. Li et al., *J. Mater. Chem. A* 6 (2018) 17889–17895.
- [97] J. Qi et al., *Chem. Soc. Rev.* 44 (2015) 6749–6773.
- [98] S. Chen et al., *Sci. China Mater.* 64 (2021) 547–556.
- [99] J.D. Mackenzie, E.P. Bescher, *Acc. Chem. Res.* 40 (2007) 810–818.
- [100] M. Niederberger, *Acc. Chem. Res.* 40 (2007) 793–800.
- [101] Y. Chen et al., *Nat. Rev. Chem.* 4 (2020) 243–256.
- [102] Q. Yu et al., *Adv. Sci.* 5 (2018) 1800782.
- [103] K. Zhang et al., *Nano Energy* 77 (2020) 105018.
- [104] C. Lv et al., *Small* 15 (2019) 1900816.
- [105] R. Hao et al., *Carbon* 128 (2018) 224–230.
- [106] S. Tian et al., *Appl. Surf. Sci.* 534 (2020) 147635.
- [107] L. Ma et al., *Nanomaterials* 11 (2021) 1130.
- [108] H. Jiang et al., *Nano-Micro Lett.* 11 (2019) 1–17.
- [109] W. Zhang et al., *Joule* 2 (2018) 1534–1547.
- [110] X. Li et al., *Nanoscale* 13 (2021) 8199–8209.
- [111] S. Wang et al., *Adv. Mater. Interfaces* 6 (2019) 1901362.
- [112] Z. Xiao et al., *Energy Environ. Sci.* 13 (2020) 3129–3137.
- [113] H. Kim et al., *Adv. Mater.* 29 (2017) 1702480.
- [114] H. Kim et al., *Adv. Energy Mater.* 7 (2017) 1700098.
- [115] X. Zhang et al., *Small* 16 (2020) 2002700.
- [116] W. Li et al., *J. Mater. Chem. A* 9 (2021) 8221–8247.
- [117] P. Li et al., *J. Mater. Chem. A* 7 (2019) 20675–20682.
- [118] X. Hu et al., *Energy Environ. Sci.* 13 (2020) 2431–2440.
- [119] D. Wu et al., *J. Mater. Chem. A* 8 (2020) 2618–2626.
- [120] H. Li et al., *Nanoscale* 12 (2020) 4309–4313.
- [121] D. Su et al., *J. Mater. Chem. A* 8 (2020) 20666–20676.
- [122] W. Miao et al., *J. Colloid Interface Sci.* 556 (2019) 432–440.
- [123] D. Liu et al., *Nano Energy* 52 (2018) 1–10.
- [124] Y. Wu et al., *Nano Lett.* 19 (2019) 1351–1358.
- [125] R. Guo et al., *Nano-Micro Lett.* 12 (2020) 1–12.
- [126] S. Tian et al., *J. Power Sources* 474 (2020) 228479.
- [127] K. Wang et al., *ACS Appl. Mater. Interfaces* 12 (2020) 37506–37514.
- [128] W. Xin et al., *RSC Advances* 11 (2021) 15416–15421.
- [129] M. Chen et al., *Adv. Funct. Mater.* 30 (2020) 2004247.
- [130] L. Xu et al., *Chem. Eng. J.* 419 (2021) 129607.
- [131] X. Xu et al., *Chem. Eng. J.* 387 (2020) 124061.
- [132] Y. Wang et al., *Nanoscale Horiz.* 4 (2019) 1394–1401.
- [133] X. Huang et al., *J. Mater. Chem. A* 8 (2020) 7641–7646.
- [134] X. Ge et al., *Angew. Chem., Int. Ed.* 58 (2019) 14578–14583.
- [135] K. Cao et al., *Adv. Mater. Technol.* 5 (2020) 2000199.
- [136] X. Xiang et al., *Appl. Surf. Sci.* 514 (2020) 145947.
- [137] K. Cao et al., *J. Electroanal. Chem.* 841 (2019) 51–55.
- [138] Z. Chen et al., *Ceram. Int.* 44 (2018) 17094–17101.
- [139] D. Su et al., *Nanoscale* 13 (2021) 6635–6643.
- [140] B. Wang et al., *J. Power Sources* 484 (2021) 229244.
- [141] R. Zhou et al., *Carbon* 186 (2022) 141–149.
- [142] Y. Wu et al., *Small* 18 (2022) 2105767.
- [143] X. Yuan et al., *Chem. Eng. J.* 405 (2020) 126897.
- [144] X. Wang et al., *Nanoscale* 9 (2017) 18216–18222.
- [145] J.H. Na et al., *Chem. Eng. J.* 425 (2021) 131651.
- [146] J. Lu et al., *ACS Appl. Mater. Interfaces* 13 (2021) 54308–54314.
- [147] S. Geng et al., *Energy Environ. Sci.* 14 (2021) 3184–3193.
- [148] C.-Y. Tsai et al., *Chem. Eng. J.* 417 (2021) 128552.
- [149] S. Intiaz et al., *Mater. Today* 48 (2021) 241–269.
- [150] D. Gong et al., *Chem. Eng. J.* 431 (2022) 133444.
- [151] X. Cheng et al., *Adv. Energy Mater.* 11 (2021) 2102263.
- [152] X. Ma et al., *Nano Energy* 24 (2016) 165–188.
- [153] A.I. Hochbaum, P. Yang, *Chem. Rev.* 110 (2010) 527–546.
- [154] X.H. Liu, J.Y. Huang, *Energy Environ. Sci.* 4 (2011) 3844–3860.
- [155] R. Xu et al., *Adv. Mater.* 32 (2020) 2003879.
- [156] Y. Yuan et al., *Nat. Commun.* 8 (2017) 15806.
- [157] H. Wang et al., *Interdiscip. Mater.* 1 (2022) 196–212.
- [158] X. Wei et al., *Small Methods* 1 (2017) 1700083.
- [159] L.-F. Cui et al., *Nano Lett.* 9 (2009) 491–495.
- [160] L.-Q. Mai et al., *Nat. Commun.* 2 (2011) 381.
- [161] Y. Shi et al., *Nano Lett.* 9 (2009) 4215–4220.
- [162] X.W. Lou et al., *Adv. Mater.* 21 (2009) 2536–2539.
- [163] L. Mai et al., *Nano Lett.* 10 (2010) 4273–4278.
- [164] X. Xu et al., *Nano Lett.* 15 (2015) 3879–3884.
- [165] P. Hu et al., *Nano Lett.* 16 (2016) 1523–1529.